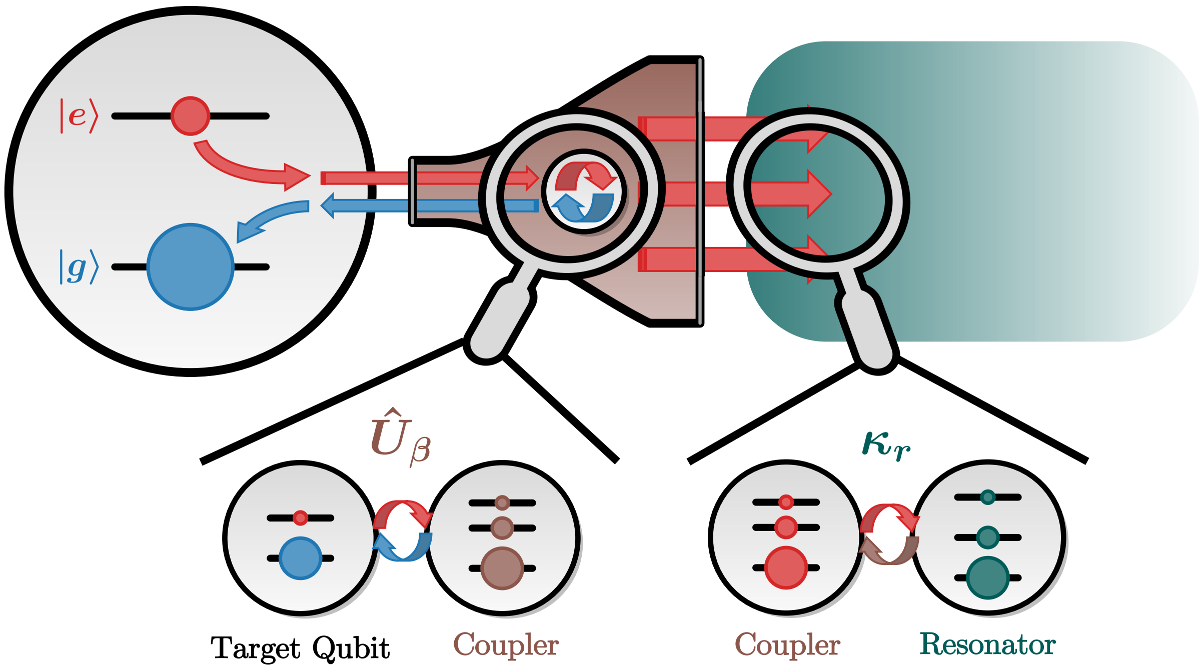

Towards Heat-Bath Algorithmic Cooling in a Superconducting Circuit

Master's thesis in Physics

OSCAR STOMMENDAL

DEPARTMENT OF MICROTECHNOLOGY AND NANOSCIENCE

CHALMERS UNIVERSITY OF TECHNOLOGY
Gothenburg, Sweden 2026
www.chalmers.se

Master's Thesis 2026

Towards Heat-Bath Algorithmic Cooling in a Superconducting Circuit

OSCAR STOMMENDAL

CHALMERS
UNIVERSITY OF TECHNOLOGY

Department of Microtechnology and Nanoscience
Division of Quantum Technology
202Q-Lab
Chalmers University of Technology
Gothenburg, Sweden 2026

Towards Heat-Bath Algorithmic Cooling in a Superconducting Circuit
OSCAR STOMMENDAL

© OSCAR STOMMENDAL, 2026.

Supervisor: Vyom Kulkarni, Chalmers University of Technology
Examiner: Simone Gasparinetti, Chalmers University of Technology

Master's Thesis 2026
Department of Microtechnology and Nanoscience
Division of Quantum Technology
202Q-lab
Chalmers University of Technology
SE-412 96 Gothenburg
Telephone +46 31 772 1000

Cover: Schematic overview of the extended heat-bath algorithmic cooling protocol.

Typeset in LaTeX
Printed by Chalmers Reproservice
Gothenburg, Sweden 2026

Towards Heat-Bath Algorithmic Cooling in a Superconducting Circuit
OSCAR STOMMENDAL
Department of Microtechnology and Nanoscience
Division of Quantum Technology
Chalmers University of Technology

Abstract

Despite being a fundamental requirement for reliable and efficient quantum computing, qubit initialization remains a major challenge, even with current state-of-the-art qubit reset techniques [1]. To address this challenge, heat-bath algorithmic cooling provides a theoretical framework for re-distributing entropy within a qubit system to initialize a subset of these into their ground states [2]. Here, we present a proof-of-concept for the experimental implementation of extended heat-bath algorithmic cooling on a superconducting two-qubit chip connected by a tunable coupler [3]. The cooling is realized through a β-SWAP, which transfers entropy from the target qubit to the coupler. To achieve optimal cooling over repeated cycles, each β-SWAP is followed by a resonator-assisted coupler re-thermalization by dissipating the extracted entropy to the environment. We experimentally demonstrate the β-SWAP and re-thermalization, achieving over 99 % population transfer for the β-SWAP and a coupler re-thermalization reaching a 4 % residual excited state population in 3 µs. Finally, we also test the full cooling protocol. From the results, we cannot observe any definite cooling effect, and the experimental data does not follow the theoretical predictions. By optimizing the device parameters and employing more advanced calibration techniques for the β-SWAP and re-thermalization, we expect to achieve the cooling effect, which would serve as an important step towards optimal qubit initialization in superconducting circuits.

Keywords: *quantum computing*, *qubit reset*, *circuit QED*, *superconducting circuits*, *quantum thermodynamics*, *algorithmic cooling.*

Acknowledgements

Firstly, I would like to thank my examiner Simone Gasparinetti for introducing me to this project, believing in my ability to carry it through, while also providing invaluable knowledge and support throughout the process. I would also like to express my sincere gratitude to my supervisor — and project partner in crime — Vyom Kulkarni, for always being generous with his time and expertise, and making every day in the lab both productive and enjoyable. To the entire 202Q-lab team, thank you for making me feel welcome from my very first day. The collaborative and friendly atmosphere you have created — from everyday discussions to after-hours barbecues — has made every day an opportunity to learn, grow, and have fun. To my friends from both my Bachelor's and Master's studies, thank you for making these years the best time of my life, including the countless hours spent deciphering Greek symbols and puzzling over equations, to the pub crawls, late nights, and unforgettable memories. Finally, to my family: Mum and Dad, thank you for always believing in me and inspiring me to become the person I am today. And to my brother, Victor, thank you for always being my best friend, helping me through difficult times, and for standing by my side every step of the way.

Oscar Stommendal, Gothenburg, July 2026

List of Acronyms

Below is the list of acronyms that have been used throughout this thesis listed in alphabetical order:

HBAC	Heat-Bath Algorithmic Cooling
QED	Quantum Electrodynamics
RF	Radio-Frequency
SNR	Signal-to-Noise Ratio
SQUID	Superconducting Quantum Interference Device

Nomenclature

Below is the nomenclature of indices, sets, parameters, and variables that have been used throughout this thesis.

Indices

i, j	General indices for states, basis elements, or summations
m	Resonator mode index or modulation label
q	Target qubit label
c	Coupler qubit label
r	Resonator label
c_r	Coupler resonator label
t	Tunable transmon label
$\star$	Optimized or calibrated value

Parameters

$\hat{H}$	Hamiltonian
Δ	Frequency detuning
g_{ij}	Coupling strength between element i and j
κ	Resonator decay rate
α	Anharmonicity
T_1	Energy relaxation time
T_2	Dephasing or coherence time
$\hat{U}_\beta^{(1/2)}$	$1^{\mathrm{st}}/2^{\mathrm{nd}}$ implemented β-SWAP term
$\tau_\beta^{(1/2)}$	β-SWAP pulse duration for $1^{\mathrm{st}}/2^{\mathrm{nd}}$ β-SWAP term
τ_{R}	Coupler re-thermalization time

Contents

List of Figures

1

Introduction

During the last decades, the field of *quantum computing* has seen rapid development. Fed by million-dollar research programs and serious investments from companies like Google, Microsoft, IBM, and Amazon, this topic has entered the discussion on all levels, from everyday living rooms to the offices of the world's most powerful people [4], [5], [6]–[9]. Quantum computing uses the principles of *quantum mechanics*, the theory describing physics on the microscopic scale, to process and distribute information in new, effective ways. By leveraging phenomena such as superposition and entanglement, quantum computers promise considerable speedups when solving certain types of problems compared to classical computers. Through these advantages, this new technology could offer potential applications within a diverse range of fields, such as cryptography, optimization, and drug fabrication.

However, current quantum processors suffer from noise and imperfect control. For instance, a major challenge for reliable quantum computing is initializing the qubits, the fundamental units of quantum information, into their ground states [1]. This project particularly focuses on *superconducting quantum circuits*, a promising platform for controlling and building quantum computers. Although superconducting circuits show major advantages, factors like finite temperatures and random qubit excitations can prevent perfect initialization and negatively impact performance. To tackle this, we study *heat-bath algorithmic cooling* (HBAC), that uses entropy redistribution as a tool to cool a superconducting qubit to its ground state.

1.1 Background

In the early 1900s, a series of crises began to erupt in physics. The problem that sparked this scientific headache was that the theories of physics at the time failed to describe and predict what the real world actually exhibited in certain events and experiments. For instance, theories of that time, now referred to as *classical physics*, predicted insanities such as energies reaching infinite values due to the "ultraviolet catastrophe", and electrons collapsing into the atomic nucleus. Naturally, many scientists desperately tried to find loopholes within classical physics to explain these perplexing observations. However, as our understanding of atoms and radiation improved, these attempts were regarded as more and more foolish. Luckily, a selection of that time's physicists took the expression "think outside the box" literally and went beyond the world of classical physics, which in this case was critical.

In the late 1920s, Bohr, Heisenberg, Schrödinger, Dirac, Born, and others had created what we today refer to as quantum mechanics — a new, revolutionary theory describing how light and matter behave at microscopic scales. Contrary to classical physics, quantum mechanics introduces several counter-intuitive phenomena that at first glance seem like science fiction. For instance, it shows that we cannot measure certain pairs of physical quantities of quantum particles with arbitrary precision (Heisenberg's uncertainty principle), and that some types of matter exhibit both wave and particle behavior (wave-particle duality). Fundamentally, all quantum systems are modeled by quantum states, often denoted $|\psi\rangle$. These are represented as n-dimensional, orthonormal (orthogonal and with length 1) vectors in Hilbert space (a mathematical structure that generalizes our three-dimensional Euclidean space to infinite dimensions). For a two-level system, this can be written as

$$|\psi\rangle = \begin{pmatrix} \alpha \\ \beta \end{pmatrix} = \alpha\,|0\rangle + \beta\,|1\rangle\,, \tag{1.1}$$

where α and β are complex numbers. This is also known as a *qubit*, which to large extent lays the foundation of this project, as we will explore later. The time evolution of such quantum states is governed by the famous Schrödinger equation,

$$i\hbar\frac{\partial}{\partial t}\,|\psi(t)\rangle = \hat{H}\,|\psi(t)\rangle\,, \tag{1.2}$$

where $\hat{H}$ is the Hamiltonian, describing the total energy of the system. The hat-notation generally indicates the presence of a *quantum operator*, representing measurable quantities, or *observables*, such as position, energy, or momentum. In quantum mechanics, observables are represented as matrices, and the measurement of an observable A on a quantum state $|\psi\rangle$ is described by the eigenvalue equation

$$\hat{A}\,|\psi\rangle = a\,|\psi\rangle\,, \tag{1.3}$$

where the number a is the measurement outcome. This also explains the name quantum mechanics, as observables only acquire discrete values, known as quanta (from Latin quantum, meaning 'amount') [10]. Since its inception, this new understanding of Nature has revolutionized modern science and technology, governing applications in areas such as lasers, MRI, and transistors.

Another pioneering application of quantum mechanics was proposed by Richard Feynman in his 1982 paper *"Simulating physics with computers"* [11]. Since Nature is undeniably built upon quantum principles, Feynman argues that quantum mechanics must be employed in order to simulate natural phenomena. This is usually cited as the first-ever mention of the field today known as quantum computing. Today, Feynman's original idea represents only one branch of the mother tree, namely *quantum technologies*, spanning everything from quantum computers to quantum sensors and quantum optics — all areas with the common goal of using quantum mechanics for fundamental technological applications. Nevertheless, quantum computing has received the most attention and has grown from a simple thought experiment into one of the most hyped research areas today.

Initially, quantum computing came into the spotlight following the discovery of quantum algorithms, such as Shor's and Grover's, that theoretically could solve problems significantly faster than their classical counterparts [12], [13]. As algorithms like these could revolutionize fields such as cryptography, optimization, and the simulation of quantum systems, they sparked a surge of interest in quantum computing. During the 2000s, focus naturally shifted to the physical realization of quantum computers, to actually harness the power of these algorithms. Today's quantum computers are still in their infancy, prone to noise and errors, and the hunt for reliable error correction and logical qubits is fully running, as we just entered the era of *fault-tolerant quantum computing*. Despite this, current devices have already demonstrated quantum supremacy, where a quantum computer can perform tasks infeasible for classical computers [14].

Due to this immense potential, we are now experiencing a race to deploy the first quantum computers, similar to the space race in the second half of the 1900s. With $10s of billions invested annually worldwide and a projected high of $72 billion in total revenues by 2035, this is a global phenomenon that shows no signs of slowing down [15]. However, despite the money and resources invested, this is easier said than done. Manipulating and controlling quantum systems is extremely difficult, and we are still in the early stages of understanding how to build practical quantum computers, as there are still many challenges to overcome.

One promising platform to realize quantum computing, and overcoming some of these challenges, is superconducting quantum circuits. These are fabricated from basic electronic components, with the so-called Josephson junction serving as the most important, and cooled to cryogenic temperatures to achieve superconductivity. This enables the creation of qubits, which are the fundamental units of quantum information. Using microwave pulses, these can be manipulated and coupled together to perform quantum gates and algorithms. Superconducting circuits come with several advantages, including their scalability and compatibility with existing semiconductor technologies. However, they also face significant challenges, including the need for extremely low temperatures and susceptibility to noise and decoherence.

This thesis explores one such challenge: qubit initialization. To perform accurate computations, the qubits must be initialized in their ground states, i.e., the state with the lowest energy [1]. In practice, this requires extremely low temperatures to minimize thermal noise and ensure the qubits remain in their desired states. However, even at temperatures as low as 50 mK, qubit excited state populations are often a coupler of percents. Furthermore, thermalizing things at very low temperatures, where the relevant interactions are heavily suppressed, also presents a crucial practical difficulty. Thus, various techniques have been developed to address this challenge. These include passive and active reset, i.e., either waiting for the qubit to relax to its initial state, or actively measure the qubit and flip the state if it is excited [16]–[19]. There are also more advanced variants, such as novel approaches based on quantum thermodynamics, for instance that demonstrated by Aamir et al., reaching record-low excited state populations [20].

Another method that has shown potential for addressing qubit initialization is the main tool explored in this project: *algorithmic cooling* [21]. This technique leverages entropy redistribution among qubits without the need of actively decreasing the temperature of the surrounding environment. In particular, we employ an extended version of so-called *heat-bath algorithmic cooling* (HBAC), that leverages a thermal environment to beat the cooling bounds of standard algorithmic cooling [2], [3]. Starting from experimentally demonstrating the individual building blocks of extended HBAC using superconducting circuits, we ultimately give a practical proposal for the implementation of the complete protocol.

1.2 Superconductivity

The concept of using superconducting circuits for realizing quantum computing would not have been possible without the work done by the Dutch physicist Heike Kamerlingh Onnes. In 1911 he discovered that, when cooled below 4.2 K, mercury almost magically lost all of its electrical resistance [22]. Today, we know this phenomena as superconductivity, which is a phase transition that many materials undergo when cooled below an element-dependent critical temperature T_c. For a long time, the underlying physics of superconductors remained a mystery, and we had to dig deep into the realm of quantum mechanics and Bose-Einstein statistics to finally understand this ground breaking phenomenon [23].

The main driving force behind superconductivity is that the electrons in a metal experiences a tiny force of attraction due to their interaction with atomic vibrations in the metal lattice (phonons) [23]. Thus, it is energetically more efficient for a pair of electrons to form a so-called *Cooper-pair* than staying one by one. The astonishing consequence of this is that such a pair of electrons, which independently are Fermi particles (fermions), instead make a Bose particle (boson). This allows the Cooper-pairs to collectively form a so-called Bose-Einstein condensate, where the breaking of one pair will change the energy of the whole structure [24]. Thus, the energy required to break one pair is related to the energy required to break all pairs in the condensate. At very low temperatures, the latter cannot be provided from the oscillating phonons, which still are the main source of energy fluctuations in this situation. Consequently, the condensate as a whole remains stable, and the total electron flow, i.e., the current, does not experience any resistance. The wave function of the real-space coordinate vector $\boldsymbol{r}$ for each Cooper-pair in the condensate can be described using the superconducting phase θ, and charge density ρ,

$$\psi(\boldsymbol{r}) = \sqrt{\rho(\boldsymbol{r})}\, e^{i\theta(\boldsymbol{r})}. \tag{1.4}$$

Unfortunately, due to the exceedingly tiny attraction force (pairing energy) only a tiny temperature is needed to break this bond, but if the temperature is made sufficiently low so that the electrons strive to reach their lowest energy state, they would appear in pairs. The temperature where this occurs is exactly the element-dependent critical temperature T_c cited above.

Since its discovery, superconductivity has opened several new research fields and applications, for instance in particle accelerators and next-generation wind turbines [25]. For this project however, the most important application of superconductors is undeniably when two superconductors, separated by an insulator, forms the so-called *Josephson junction*. This element plays a crucial part in the creation of the non-linear circuit elements that is the foundation of superconducting qubits.

1.2.1 The Josephson Effect

The aforementioned Josephson junction is based on the phenomenon first described by Brian Josephson in 1962, for which he received the Nobel prize in 1973 [26], [27]. This discovery is known today as the Josephson effect. It occurs when two superconductors, separated by a thin insulator, exchanges current in the form of electron Cooper-pairs which tunnel through the insulator barrier. Figure 1.1 below schematically describes the structure of a Josephson junction.

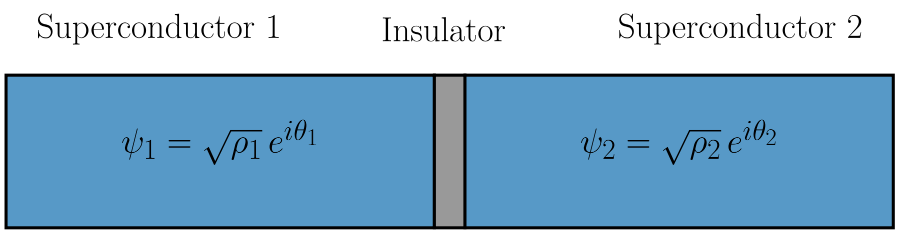

Figure 1.1: A simple sketch of the Josephson junction. Two superconductors, described by the Bose-Einstein condensate wave function, allows current to tunnel through the thin, separating insulator layer.

Using the BEC wave function from the previous section for each superconductor, we can define the phase between these as $\gamma = \theta_1 - \theta_2$. The voltage and current for this structure can be derived by solving the coupled Schrödinger equation of the two wave functions ψ_1 and ψ_2 [23], which gives

$$I_J = I_c \sin(\gamma(t)) \tag{1.5}$$

$$\frac{d\gamma(t)}{dt} = \frac{2e}{\hbar} V_J = \frac{2\pi}{\Phi_0} V_J. \tag{1.6}$$

Here, I_c the element-dependent critical current, at which a certain material loses its superconductivity, and $\Phi_0 = h/2e$ is the magnetic flux quantum, which is the quantized amount of magnetic flux flowing through a superconductor. From these expressions, we can also derive the Josephson junction inductance,

$$L_J(\gamma) = V_J \left(\frac{dI_J}{dt}\right)^{-1} = \frac{\Phi_0}{2\pi I_c \cos(\gamma)}. \tag{1.7}$$

The most important result here is that the inductance is, in courtesy of the cosine term, non-linear, allowing us to create non-linear circuit elements. This is essential for the creation of superconducting qubits, which lays the foundation of this project.

2

Theory

This chapter aims to provide the necessary theoretical foundations for the thesis. We start from the framework describing quantum systems in the presence of an external environment, i.e., *open quantum systems*, including the Lindblad master equation, noise channels, and thermal populations. Next, the quantization of superconducting circuits is covered by deriving the standard and flux-tunable transmon qubit from the classical LC oscillator. From there, we describe the study of superconducting circuits and electromagnetic fields in the microwave-frequency domain, i.e., circuit quantum electrodynamics (QED). Finally, algorithmic cooling is described in detail, and especially the main focus of this thesis: HBAC. The first three main sections of this chapter are already extensively covered in literature, see for instance [28] for open quantum systems, and [29] and [30] for superconducting circuits and circuit QED. The primary focus of this chapter will therefore be to introduce algorithmic cooling and extended HBAC, especially in the setting of superconducting circuits.

2.1 Open Quantum Systems

When studying real-world quantum mechanical systems, one often has to consider their interaction with some surrounding environment, see Figure 2.1. This generally increases complexity compared to closed systems as it allows system information to vanish. In the context of HBAC, which explicitly employs an external heat bath, such systems are pivotal. Luckily, a framework for describing this exists: open quantum systems. From the introduction chapter, we know that a quantum state can be described using a state vector $|\psi\rangle$. For the modeling of open quantum systems, however, it is more convenient to define the so-called *density matrix*,

$$\hat{\rho} = \sum_i w_i \, |\psi\rangle_i \, \langle\psi|_i \, , \tag{2.1}$$

where $w_i \geq 0$ are weights satisfying $\sum_i w_i = 1$ [28]. This can be understood as a statistical mixture of quantum states, where w_i is the fraction of state $|\psi\rangle_i$ in the ensemble. In principle, $\hat{\rho}$ is a generalization of $|\psi\rangle$, as the latter only describe so-called *pure states*, whereas the former extends to also cover *mixed states*, which often arise in open systems. From here, we also define the *von-Neumann entropy*,

$$S = -\mathrm{tr}(\hat{\rho} \ln(\hat{\rho})), \tag{2.2}$$

where tr $(\cdot)$ denotes the trace [28]. This is vital in the context of algorithmic cooling and represents the uncertainty about which specific state $|\psi\rangle_i$ is present in the mixture. For instance, the von-Neumann entropy assumes its minimum $S = 0$ for a pure state, and maximum $S = \log(N)$ for a maximally mixed state, where N is the dimension of the Hilbert space ($N = 2$ for a qubit system). For the system shown in Figure 2.1, it is also possible to express the composite density matrix $\hat{\rho}_C$ as

$$\hat{\rho}_C = \hat{\rho}_S \otimes \hat{\rho}_E, \tag{2.3}$$

where $(\cdot \otimes \cdot)$ denotes the *Kronecker product*. If the system and environment are described by Hilbert spaces $\mathcal{H}_S$ and $\mathcal{H}_E$, respectively, then $\hat{\rho}_C$ will live in the combined space $\mathcal{H}_S \otimes \mathcal{H}_E$. Consequently, by taking the *partial trace* over the system or environment, we return to $\hat{\rho}_S$ and $\hat{\rho}_E$ again, often referred to as *reduced density matrices* in the context of composite systems. For S, this would be expressed as

$$\hat{\rho}_S = \sum_i (I_S \otimes \langle i|_E)\hat{\rho}_C(I_S \otimes |i\rangle_E), \tag{2.4}$$

where I_S is the identity matrix in $\mathcal{H}_S$ and $\{|i\rangle_E\}$ is an orthonormal basis for $\mathcal{H}_E$.

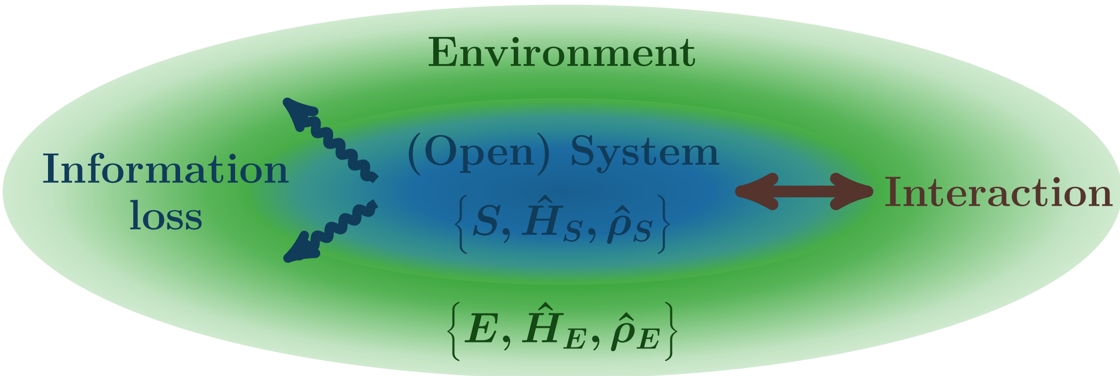

Figure 2.1: Schematic picture of an open quantum system S interacting with an environment E, each described by a Hamiltonian $\hat{H}$ and density matrix $\hat{\rho}$. The wavy arrows represents information loss from the system S to the environment E.

In contrast to closed systems, the time evolution of open systems cannot be described using the Schrödinger equation [28]. Instead, one must employ certain approximations to model this in the realm of open systems. One approach, when the system-environment interaction is weak, is through perturbation theory, meaning that changes over time of the combined system $S + E$ can be approximated only from the system S in question. Another common approximation is the concept of Markovianity. A Markovian system has an environment that is said to act *memoryless*, meaning that the future time evolution is independent of its history. When these two approximations are valid, we arrive at the *Lindblad master equation*. Similar to the relation between $\hat{\rho}$ and $|\psi\rangle$, this is a generalization of the Schrödinger equation, also covering the time evolution of the density matrix,

$$\frac{d}{dt}\hat{\rho}_S = -\frac{i}{\hbar}\left[\hat{H}, \hat{\rho}_S\right] + \sum_n \Gamma_n \left(\hat{L}_n \hat{\rho}_S \hat{L}_n^\dagger - \frac{1}{2}\left\{\hat{L}_n^\dagger \hat{L}_n, \hat{\rho}_S\right\}\right). \tag{2.5}$$

Here, $\hat{H}$ is a hermitian operator describing the coherent (closed) part of the dynamics (this includes $\hat{H}_S$, and can also involve additional terms from the system-environment interaction), $[\hat{a}, \hat{b}] = \hat{a}\hat{b} - \hat{b}\hat{a}$ and $\{a, b\} = \hat{a}\hat{b} + \hat{b}\hat{a}$ are the commutator and anti-commutator, $\{\hat{L}_i^\dagger, \hat{L}_i\}$ are so-called jump-operators, describing the dissipative part of the dynamics, and Γ_i is the decay rate associated with each jump-operator. In other words, the jump-operators describe the environment's actions on the system and the decay rates correspond to the duration of each action.

2.1.1 Quantum Decoherence

The information loss arising from the interaction between a quantum system and an environment is known as *quantum decoherence*. In this thesis, where we have a qubit coupled to an external environment, the main sources of decoherence are *dephasing*, *relaxation*, and *excitation*. These are represented by the jump-operators

$$\hat{\sigma}_z = \begin{pmatrix} 1 & 0 \\ 0 & -1 \end{pmatrix}, \quad \hat{\sigma}_- = \begin{pmatrix} 0 & 1 \\ 0 & 0 \end{pmatrix}, \quad \hat{\sigma}_+ = \begin{pmatrix} 0 & 0 \\ 1 & 0 \end{pmatrix}, \tag{2.6}$$

with decay rates Γ_ϕ, Γ_-, and Γ_+. From these, we define the relaxation and dephasing rates Γ_1 and Γ_2 with corresponding relaxation and coherence times T_1 and T_2,

$$\Gamma_1 = \frac{1}{T_1} = \Gamma_- + \Gamma_+, \tag{2.7}$$

$$\Gamma_2 = \frac{1}{T_2} = \frac{1}{2T_1} + \Gamma_\phi. \tag{2.8}$$

These are central in the characterization of superconducting qubits, where higher relaxation times often means more stable and high-quality qubits. The action of these operators can be understood as follows. The dephasing operator $\hat{\sigma}_z$ causes a loss of coherence, i.e., the non-classical phase correlation, between state $|g\rangle$ and $|e\rangle$ of a qubit. This results in a decay of the off-diagonal elements of the density matrix, leading to a mixed state. The relaxation operator $\hat{\sigma}_-$ causes a transition from the excited state $|e\rangle$ to the ground state $|g\rangle$, resulting in system energy loss. This could for instance happen when the surrounding environment is colder than the qubit, causing energy to flow from the qubit to the environment. Similarly, the excitation operator $\hat{\sigma}_+$ is equivalent to an excitation in the qubit, i.e., a transition from $|g\rangle$ to $|e\rangle$. This can be interpreted as energy absorption from the environment, which could be a consequence of a warmer environment, in analogy to relaxation.

2.1.2 Thermal Populations

The algorithmic cooling protocol requires an external environment in thermal equilibrium. Within open quantum systems, this is often referred to as a heat bath [28]. In this project, the heat bath is realized by using a so-called waveguide resonator. A resonator, or *bosonic mode*, of angular frequency ω at temperature T has an average thermal photon occupation given by the Bose–Einstein distribution,

$$n_P(\omega, T) = \frac{1}{e^{\hbar\omega/k_B T} - 1}, \tag{2.9}$$

where k_B is Boltzmann's constant. The relevance of n_P for a qubit can be derived from the Lindblad master equation for a two-level system coupled to a thermal bosonic bath. For a qubit transition frequency ω_q, the downward (de-excitation) and upward (excitation) transition rates are

$$\Gamma_\downarrow = \gamma(\omega_q)\left[n_P(\omega_q, T) + 1\right], \tag{2.10}$$

$$\Gamma_\uparrow = \gamma(\omega_q) n_P(\omega_q, T), \tag{2.11}$$

where $\gamma(\omega_q)$ depends on the bath spectral density and the qubit–bath coupling at the transition frequency. The excited-state population P_e then obeys $\dot{P}_e = \Gamma_\uparrow(1 - P_e) - \Gamma_\downarrow P_e$. In steady state, i.e., where $\dot{P}_e = 0$, this gives

$$P_e^{\mathrm{ss}} = \frac{\Gamma_\uparrow}{\Gamma_\uparrow + \Gamma_\downarrow} = \frac{n_P(\omega_q, T)}{2n_P(\omega_q, T) + 1} = \frac{1}{e^{\hbar\omega_q/k_B T} + 1}. \tag{2.12}$$

Thus, although the bath itself is bosonic, the thermal excited-state population of a two-level system takes the form of a Fermi–Dirac-like distribution.

2.2 Superconducting Qubits

The first crucial ingredient for this project are superconducting qubits, which can be understood as artificial atoms realized using superconducting quantum circuits. One of the earliest realizations of this is the Cooper-pair box, where Cooper-pairs tunnel onto and off a superconducting island [31]. While this demonstrates the basic operating principle, it is highly sensitive to charge noise. A more robust implementation, and the main tool used in this project, is the *transmon qubit*, which adds a large shunting capacitance to suppress charge fluctuations while maintaining the behavior of a qubit [32]. This section starts by describing the classical LC oscillator, which naturally translates to the transmon through the *quantization* of the LC circuit. Finally, we also discuss the utilization of Superconducting Quantum Interference Devices (SQUIDs) to implement *flux-tunable transmons.*

2.2.1 The Harmonic LC Oscillator

When addressing problems in physics, independently of complexity, it is usually beneficial to start from known models. This is particularly true when studying quantum mechanics, as it often appears less intuitive than classical physics. Here, we leverage exactly this. Starting from the classical LC oscillator, which dynamics is well-known, we will translate this to a quantum picture. This lets us describe more complex circuits that are essential for superconducting quantum circuits, ultimately leading to a crucial part of the core of this project: the transmon qubit.

The classical LC oscillator, described by its inductance L and capacitance C, vibrates at its resonant frequency $\omega_r = 1/\sqrt{LC}$. Physically, these oscillations are caused by energy fluctuations between the magnetic field of the inductor and the electrical field of the capacitance. The Hamiltonian of this system can be defined as the sum of the inductive and charge energy [29],

$$\hat{H}_{LC} = \frac{\hat{\Phi}^2}{2L} + \frac{\hat{Q}^2}{2C}. \tag{2.13}$$

Here, Φ is the magnetic flux of the inductor and Q the charge on the capacitor. To translate this into a quantum mechanical description, the first step is to define the observables of the system. In this case, it is convenient to use the aforementioned flux Φ and charge Q of the LC circuit. From this, we introduce the creation and annihilation operators of the classical harmonic oscillator, $\hat{a}^\dagger$ and $\hat{a}$,

$$\hat{a}^\dagger,\, \hat{a} = \sqrt{\frac{\omega_r C}{2\hbar}}\,\hat{\Phi} \mp \frac{i}{\sqrt{2\hbar\omega_r C}}\,\hat{Q}. \tag{2.14}$$

Physically, these operators represents the creation ($\hat{a}^\dagger$) and annihilation ($\hat{a}$) of a photon (the quantized unit of light) with frequency ω_r inside the circuit. But, most importantly, this allows us to rewrite the Hamiltonian in Equation 2.13 as

$$\hat{H}_{LC} = \hbar\omega_r(\hat{a}^\dagger\hat{a} + \frac{1}{2}). \tag{2.15}$$

This describes a *quantum harmonic oscillator*, with eigenstates $\hat{a}^\dagger\hat{a}\,|n\rangle = n\,|n\rangle$ and energies $E_n = \hbar\omega_r(n + 1/2)$ for $n = 0, 1, 2, \ldots$. Figure 2.2 shows the corresponding energy level spectrum, characterized by an equal spacing between consecutive levels. This is a consequence of the fact that inductors and capacitors are linear circuit elements, meaning that the output is directly proportional to the input. To create a qubit however, we need energy levels with different, distinguishable energy spacings. For this, we will utilize the non-linear Josephson junction introduced in Chapter 1.

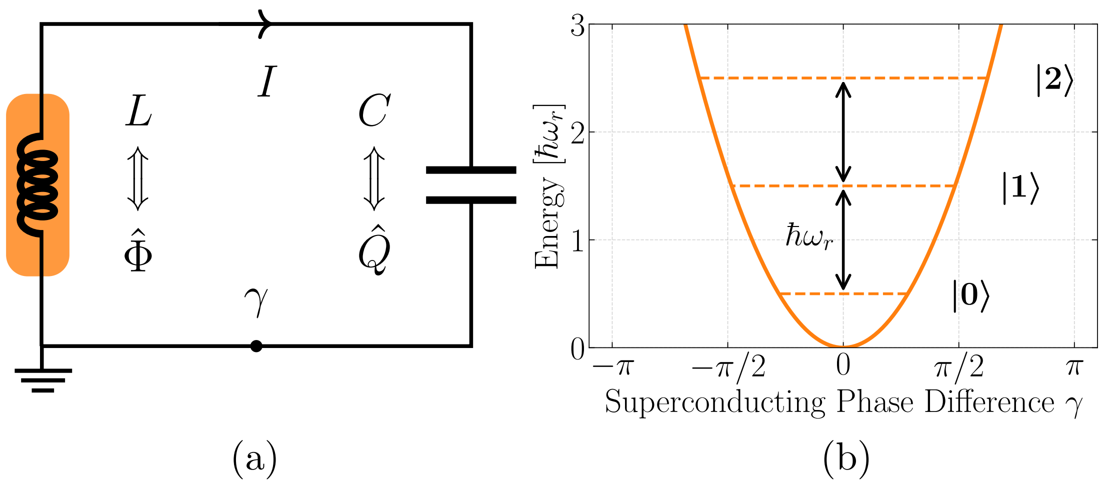

Figure 2.2: (a) Circuit diagram of the LC circuit. (b) Energy level spectrum of the LC circuit, showing the equal spacing between consecutive energy levels.

2.2.2 The Transmon Qubit

We are now ready to create an actual, or at least theoretical, superconducting qubit. By replacing the inductor in the LC circuit with a Josephson junction, non-linearity is introduced in the system, see Figure 2.3. Using Equations 1.5–1.7 for the Josephson current, voltage, and inductance, the circuit Hamiltonian can be written as

$$\hat{H} = 4E_C\hat{n}^2 - E_J\cos(\hat{\gamma}). \tag{2.16}$$

Here, $\hat{n} = \hat{Q}/2e$ is the charge number operator, $\hat{\gamma} = 2\pi\hat{\Phi}/\Phi_0$ the superconducting phase operator, $E_J = \Phi_0 I_c/2\pi$ the Josephson energy, and $E_C = e^2/2(C_J + C_S)$ the charging energy, with C_J and C_S as the JJ and shunt capacitances, respectively [29]. The ratio E_J/E_C is critical for controlling the energy spectrum of the circuit, where different values correspond to different kinds of qubits [33]. In this thesis, we focus on so-called transmon qubits, which are realized when choosing a large E_J/E_C ratio, typically $E_J/E_C \sim 20-80$, by increasing the shunt capacitance C_S. The main reason behind this is to minimize charge noise, i.e., changes in energy due to circuit charge fluctuations, which is proven harder to deal with than flux noise.

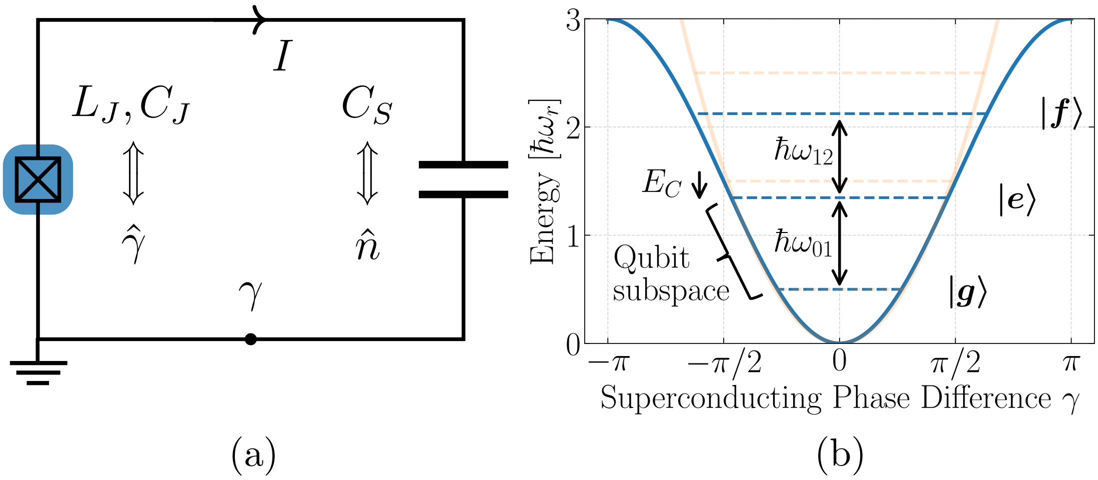

Figure 2.3: (a) Transmon circuit diagram, where the inductor of the LC circuit is replaced by a Josephson junction. (b) Corresponding energy level spectrum, showing the anharmonicity α that allows us to treat the two lowest levels as a qubit.

As the phase γ is small in this regime, we can expand the cosine-term in a power series. Keeping terms up to fourth order, we can rewrite Equation 2.16 according to

$$\hat{H}_T = \hbar\omega_q\hat{b}^\dagger\hat{b} + \frac{\alpha}{2}\hat{b}^\dagger\hat{b}^\dagger\hat{b}\hat{b}, \tag{2.17}$$

where $\omega_q = \sqrt{8E_CE_J} - E_C$ is the transmon frequency and $\alpha = -E_C$ the *anharmonicity*. We have also introduced creation and annihilation operators $\hat{b}^\dagger$ and $\hat{b}$ in analogy to the quantum harmonic oscillator Hamiltonian in Equation 2.15,

$$\hat{b}^\dagger,\, \hat{b} = \frac{1}{2}\left(\frac{E_J}{2E_C}\right)^{1/4}\hat{\phi} \mp i\left(\frac{2E_C}{E_J}\right)^{1/4}\hat{n}. \tag{2.18}$$

Comparing Equation 2.17 to that of the quantum harmonic oscillator in Equation 2.15, we see that the transmon essentially is an anharmonic oscillator, in courtesy of α. Figure 2.3 shows the circuit diagram of the transmon, and the resulting energy diagrams. Compared to the quantum harmonic oscillator, the anharmonicity allows us to independently access the first and second eigenstate, often referred to as $|g\rangle$ and $|e\rangle$, as our qubit, since the levels are no longer evenly separated. However, it is important to remember that this is not an ideal two-level system, and that higher order states also exist.

2.2.3 Flux-Tunable Transmons

A useful variant of the transmon can be realized when coupling two Josephson junctions in parallell, creating a SQUID, see Figure 2.4 below [32]. By applying an external magnetic flux Φ_e, the phase differences across the two junctions are constrained by the flux quantization condition (i.e., that it is quantized in units of 2π), allowing us to treat this as a single Josephson junction [30]. This is described by the Hamiltonian

$$\hat{H}_{TT} = 4E_C\hat{n}^2 - 2E_J\cos(\gamma_e)\cos(\hat{\gamma}), \tag{2.19}$$

where $\gamma_e = \pi\Phi_e/\Phi_0$ is the additional contribution to the superconducting phase from Φ_e. This expression is directly analogue to the fixed-frequency transmon Hamiltonian in Equation 2.16, but with the new, tunable Josephson energy $E_J' = 2E_J\cos(\varphi_e)$, creating a *flux-tunable transmon*. The right panel of Figure 2.4 shows the tunable transmon frequency ω_{01} as a function of the external flux. Here, it is important to notice that a steeper slope results in a larger frequency shift from small deviations in Φ_e. Thus, the ideal parking for the tunable transmon frequency are one of the peaks where the slope is negligible, often called "sweet spots".

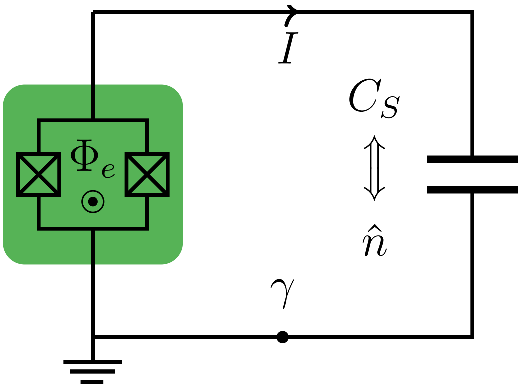

(a)

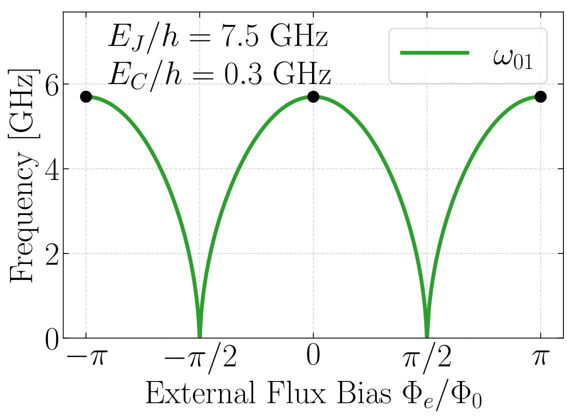

(b)

Figure 2.4: (a) Circuit diagram for a flux-tunable transmon. (b) The first transition frequency, corresponding to that of a qubit as a function of the external flux through the SQUID loop. The black dots indicate the sweet spots.

2.3 Circuit Quantum Electrodynamics

In analogy to how previous sections answered questions on how superconducting qubits are realized, the following aims to explain how these are controlled and measured. This is often described in the framework of circuit QED, which is the study of the interaction between superconducting qubits and microwave photons. The most crucial components in circuit QED are radio frequency (RF) waves and so-called *coplanar waveguide resonators*, which can be can be understood as two-dimensional signal lines. Here, we start by describing the latter, which fills multiple important purposes in this project. The RF waves essentially act as the means of communicating with the qubits. For this, we will employ the Jaynes-Cummings Hamiltonian, which describes the interaction between quantized electromagnetic waves and atoms. Finally, the relevant interactions between combinations of elements, that is qubit-qubit and qubit-resonator couplings, are modeled.

2.3.1 Coplanar Waveguide Resonators

Harmonic oscillators can be realized from several different geometries and structures, where the aforementioned LC-oscillator is one example. Another type is the coplanar waveguide resonator, or just resonator for short, which can be seen as a two-dimensional coaxial transmission line consisting of capacitors and inductors coupled in parallel, see Figure 2.5 [29]. The structure of resonators allows for the creation of quantized modes of the electromagnetic field (photons) within the resonator, ultimately enabling us to use these as a resource for controlling and measuring qubits.

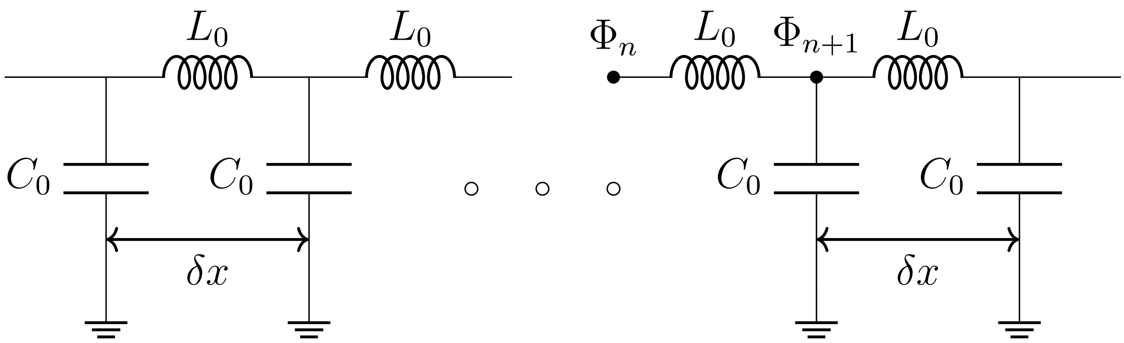

Figure 2.5: Circuit model of a coplanar waveguide resonator, consisting of capacitors and inductors coupled in parallel in unit cells with size δx.

In the x-direction, the electromagnetic wave propagation can be modeled using a one-dimensional, dispersion-free medium. For this purpose, we start from the classical Hamiltonian describing the circuit in Figure 2.5,

$$\hat{H}_{CWR} = \sum_{n=0}^{N-1} \left(\frac{1}{2C_0} \hat{Q}_n^2 + \frac{1}{2L_0} \left(\hat{\Phi}_{n+1} - \hat{\Phi}_n \right)^2 \right), \tag{2.20}$$

where $\hat{Q}$ and $\hat{\Phi}$ are the same operators used in the LC circuit Hamiltonan in Equation 2.13. From here, we consider the continuum limit of this structure, meaning that the size of a unit cell in the circuit, δx, is taken to 0. Using Hamilton's equation for this configuration, the wave propagation along the line can be described by

$$v_0^2 \frac{\partial^2 \hat{\Phi}(x,t)}{\partial t^2} - \frac{\partial^2 \hat{\Phi}(x,t)}{\partial x^2} = 0, \tag{2.21}$$

where v_0 is the speed of light in the medium. The solution can be expressed as

$$\hat{\Phi}(x,t) = \sum_{m=0}^{\infty} u_m(x) \hat{\Phi}_m(t), \tag{2.22}$$

where $u_m(x) = A_m \cos(k_m x + \varphi_m)$. Here, the wave vector k_m and phase φ_m are determined from the boundary conditions. By choosing these appropriately, the electromagnetic field is decomposed into a discrete set of allowed modes, each behaving as an independent harmonic oscillator with its own resonance frequency. Therefore, different boundary conditions give rise to different types of resonators. For instance, open-ended resonators requires that the current vanishes at both line ends, whereas shorted requires vanishing voltage. Generally, however, the resonator Hamiltonian can be written as a sum over independent harmonic modes,

$$\hat{H}_{CWR} = \sum_{m=0}^{\infty} \hbar\omega_m \left(\hat{a}_m^\dagger \hat{a}_m + \frac{1}{2} \right). \tag{2.23}$$

where ω_m is the mode frequency and $\hat{a}_m^\dagger$ ($\hat{a}_m$) is the photon creation (annihilation) operator of each mode, in analogy to the quantized LC oscillator in Equation 2.15. In the scope of this thesis, however, we are only interested in the fundamental mode $m = 0$, which reduces Equation 2.23 to the Hamiltonian of a single quantum harmonic oscillator. Ultimately, by coupling a qubit to a resonator, the photons inside the resonator can be used as a resource for controlling and measuring the qubit. Furthermore, in the context of HBAC, resonators also play the crucial role of the heat bath. By using a resonator with a quick photon decay to the external environment, entropy can effectively be removed from the system.

2.3.2 The Jaynes-Cummings Hamiltonian

In circuit QED, the resonators introduced in the last section are employed to measure and control superconducting qubits. In practice, this is realized by coupling a resonator to a qubit while sending photons via the resonator to the qubit. From the resonator-qubit coupling, the resonator can be utilized to measure the state of the qubit, while the latter serves as qubit control. By truncating the resonator to include only one mode, and the transmon to its first two levels, the interaction between this and a resonator is described by the *Jaynes-Cummings (JC) Hamiltonian*,

$$\hat{H}_{JC} = \hbar\omega_r \left(\hat{a}^\dagger \hat{a} + \frac{1}{2} \right) + \frac{\hbar\omega_q}{2} \hat{\sigma}_z + \hbar g (\hat{a}^\dagger \hat{\sigma}_- + \hat{a} \hat{\sigma}_+). \tag{2.24}$$

Here, ω_r and ω_q is the resonator and qubit frequency, respectively, g the coupling strength, and $\hat{\sigma}_z$, $\hat{\sigma}_-$, and $\hat{\sigma}_+$ are the qubit Pauli-Z, lowering and raising operators. These are equivalent to the dephasing, relaxation, and excitation jump-operators in Section 2.1.1. We recognize the first term as the quantum harmonic oscillator Hamiltonian, here describing the resonator. Together with the second term, which is the bare qubit Hamiltonian, this models the free (interaction-less) system evolution. The last term is the interaction-term, allowing for energy exchange between the qubit and resonator. The $\hat{a}^\dagger\hat{\sigma}_-$ term corresponds to the exchange where a resonator photon is created from the relaxation (energy-loss) in the qubit, and vice versa for $\hat{a}\hat{\sigma}_+$. Ultimately, this enables us to control and measure the qubit state using photons in the resonator, as described in the next section.

2.3.3 Controlling and Measuring Superconducting Qubits

With the JC Hamiltonian, we have the foundational ingredient for understanding how to control and measure our transmons. By coupling these to resonators, electromagnetic pulses (photons) can be applied through the resonators and used as a resource for both qubit control and measurement. Here, we start by introducing *dispersive readout*, which is the most common measuring technique used in today's circuit QED designs. Subsequently, we describe the coupling between qubits and other circuit elements in this regime, including resonators and tunable transmons. This lays the foundation for qubit control, especially in the context of HBAC.

2.3.3.1 Dispersive Readout

The concept of dispersive readout revolves around a qubit coupled to a resonator in the *dispersive regime*, characterized by $\Delta \gg g$, where the *detuning* $\Delta = |\omega_q - \omega_r|$. Contrary to when $\Delta \ll g$, the dispersive regime does not allow any direct energy exchange between the two systems, allowing us to measure the qubit state without disturbing it simultaneously. The dispersive regime instead force the resonator and qubit frequency to "push" each other, allowing us to infer the state of the qubit from that of the resonator. Thus, we are able to map the quantum state onto the classical response of the linear resonator, and the readout optimization is essentially a question of obtaining the best signal-to-noise ratio (SNR).

What we describe above can also be expressed from a mathematical point of view. By performing the dispersive approximation $\Delta \gg g$ on the JC Hamiltonian in Equation 2.16, we find the dispersive Hamiltonian

$$\hat{H}_{\text{disp}} = \hbar\omega_r\hat{a}^\dagger\hat{a} + \frac{\hbar\omega_q}{2}\hat{\sigma}_z + \hbar\chi\hat{a}^\dagger\hat{a}\hat{\sigma}_z, \tag{2.25}$$

where $\chi = -g^2/\Delta$ is the qubit state-dependent dispersive resonator shift. Here, it is important to note that the JC Hamiltonian describes a perfect qubit coupled to a resonator. If the third transmon level is included in the dispersive approximation, χ is instead given by $\chi = g^2E_C/(\Delta(\Delta - E_C))$.

In either case, this physically means that the resonator frequency ω_r is shifted by χ depending on if the qubit is in state $|g\rangle$ or $|e\rangle$. The value of χ is therefore crucial for distinguishing the two qubit states, where a larger χ results in better state read out. For a fixed qubit-resonator coupling g, however, increasing χ is equivalent to decreasing the *critical photon number* $n_c = \Delta^2/4g^2$, which defines the maximal input power that can be applied to the resonator without breaking the dispersive approximation. Thus, there is a trade-off between increasing χ and maintaining the dispersive regime, which is crucial for optimizing the readout performance.

2.3.3.2 Tunable-Transmon-Qubit Coupling

To implement HBAC in a superconducting circuit, there are two crucial interaction types between circuit elements that we must understand. These are the tunable transmon-qubit and tunable transmon-resonator couplings, which we will now describe. The interaction between a tunable transmon and fixed-frequency transmon (qubit) can be modeled using the composite system basis $|QT\rangle = |Q\rangle_q \otimes |T\rangle_t$, with $Q = g, e, f, \ldots$ and $T = 0, 1, 2, \ldots$ [34], [35]. After truncating the system to the first three levels, the Hamiltonian can be approximated by

$$\begin{aligned}\hat{H}/\hbar = \mathbb{1}_q \otimes (\omega_t(t)|1\rangle\langle 1|_t + (2\omega_t(t) + \alpha_t)|2\rangle\langle 2|_t) \\ + \left(\omega_q|e\rangle\langle e|_q + (2\omega_q + \alpha_q)|f\rangle\langle f|_q\right) \otimes \mathbb{1}_t + g_{qt}\left(\hat{\sigma}_q^\dagger \otimes \hat{\sigma}_t + \hat{\sigma}_q \otimes \hat{\sigma}_t^\dagger\right).\end{aligned} \tag{2.26}$$

Here, $\omega_t(t)$ (ω_q) is the tunable transmon (qubit) frequency, α_t (α_q) the corresponding anharmonicity, $\mathbb{1}_t$ ($\mathbb{1}_q$) the identity operator in the tunable transmon (qubit) subspace, g_{qt} the tunable transmon-qubit coupling strength, and $\hat{\sigma}_{q(t)} = |g(0)\rangle\langle e(1)|_{q(t)} + \sqrt{2}|e(1)\rangle\langle f(2)|_{q(t)}$ are the operators describing the energy exchange of the interaction. When modulating the flux through the tunable transmon, its time-dependent frequency can be modeled as

$$\omega_t(t) = \overline{\omega}_t + A_m \sin(\omega_m t + \theta_m), \tag{2.27}$$

where A_m, ω_m, and θ_m are the modulation amplitude, frequency, and phase, respectively, and $\overline{\omega}_t = \omega_t + \delta t$ is the average tunable transmon frequency during the modulation. When moving into the rotating frame governed by Equation 2.27, the interaction Hamiltonian for the system is given by (omitting irrelevant terms)

$$\begin{aligned}\hat{H}_{\text{int}}^{qt}/\hbar = \sum_{n=-\infty}^{\infty} g_n \Big[e^{i(n\omega_m - \Delta_{qt})t}|g1\rangle\langle e0| \\ + \sqrt{2}\, e^{i(n\omega_m - [\Delta_{qt} - \alpha_q])t}|e1\rangle\langle f0| + \sqrt{2}\, e^{i(n\omega_m - [\Delta_{qt} + \alpha_t])t}|g2\rangle\langle e1| + \text{h.c.}\Big].\end{aligned} \tag{2.28}$$

Here, $\Delta_{qt} = \omega_q - \overline{\omega}_t$ is the modulation detuning, and $g_n = g_{qt}\, \mathrm{J}_n(A_m/\omega_m)\, e^{i\beta_n}$, with β_n and $\mathrm{J}_n(x)$ as the interaction phase and first-order Bessel functions, are the effective coupling strengths. Below, the interaction between a tunable transmon and resonator is theorized in a similar manner.

2.3.3.3 Tunable-Transmon-Resonator Coupling

Equally important to the previous tunable transmon-qubit interaction, will be that of a tunable transmon coupled to a resonator. Similarly to the tunable transmon-qubit system, we now consider the composite tunable-transmon-resonator system, with basis states $|RT\rangle = |R\rangle_r \otimes |T\rangle_t$. Following the derivation by Zhou et al., the truncated 3-level Hamiltonian of this system takes a similar form as the tunable transmon-qubit Hamiltonian in Equation 2.26 [36],

$$\begin{aligned}\hat{H}/\hbar = & \mathbb{1}_t \otimes (\omega_r |1\rangle\langle 1|_r + 2\omega_r |2\rangle\langle 2|_r) \\ & + (\omega_t |1\rangle\langle 1|_t + (2\omega_t + \alpha_t)|2\rangle\langle 2|_t) \otimes \mathbb{1}_r + g_{tr}\left(\hat{\sigma}_t^\dagger \otimes \hat{\sigma}_r + \hat{\sigma}_t \otimes \hat{\sigma}_r^\dagger\right).\end{aligned} \tag{2.29}$$

Here, ω_r is the resonator frequency, g_{tr} the tunable transmon-resonator coupling strength, and $\hat{\sigma}_{r(t)} = |0\rangle\langle 1|_{r(t)} + \sqrt{2}|1\rangle\langle 2|_{r(t)}$ are again the energy exchange operators. During flux modulation, the tunable transmon frequency will again follow the time dependence defined in Equation 2.27. The interaction Hamiltonian in that rotating frame for the tunable transmon-resonator system will then be given by

$$\begin{aligned}\hat{H}^{tr}_{\text{int}}/\hbar = & \sum_{n=-\infty}^{\infty} g_n \Big[e^{i(n\omega_m - \Delta_{rt})t} |01\rangle\langle 10| \\ & + \sqrt{2}\, e^{i(n\omega_m - \Delta_{rt})t} |11\rangle\langle 20| + \sqrt{2}\, e^{i(n\omega_m - [\Delta_{rt} - \alpha_t])t} |02\rangle\langle 11| + \text{h.c.} \Big].\end{aligned} \tag{2.30}$$

In analogue to the tunable transmon-qubit interaction Hamiltonian in Equation 2.28, $\Delta_{rt} = \omega_r - \overline{\omega}_t$ is the modulation detuning, and $g_n = g_{tr}\, \mathrm{J}_n(A_m/\omega_m)\, e^{i\beta_n}$ are the effective coupling strengths of this interaction.

2.4 Algorithmic Cooling

Algorithmic cooling was theoretically proposed in the early 2000s and leverages the redistribution of entropy within a set of qubits, with the goal of cooling a subset of these to their ground state. The first version of algorithmic cooling was formulated as a "*molecular scale heat engine*" by Schulman and Vazirani in 1999 [21]. This version is *reversible*, meaning that the total system entropy remains fixed throughout the protocol execution. Quantum mechanically, this would be equivalent to a closed system. Shortly after, standard algorithmic cooling was extended to the main tool explored in this thesis: heat-bath algorithmic cooling (HBAC), proposed by Boykin et al. in 2001 [2]. Contrary to standard algorithmic cooling, this variant is *irreversible* and described using open quantum systems as an external, thermally equilibrated environment (heat bath) is applied to remove entropy from the target system more efficiently. Theoretically, this allows for reaching lower target temperatures. Starting from standard algorithmic cooling, the following aims to explain the theoretical aspect of HBAC, and particularly how the extended version proposed by Àlhambra et al. could be implemented in a superconducting circuit [3].

2.4.1 Reversible Algorithmic Cooling

As mentioned, the main tool used in both regular algorithmic cooling and the HBAC-extension is the redistribution of entropy — more specifically the von-Neumann entropy — defined in Equation 2.2. In the context of algorithmic cooling, the general qubit state of interest can be expressed using the density matrix,

$$\hat{\rho}(\varepsilon) = \begin{pmatrix} \frac{1+\varepsilon}{2} & 0 \\ 0 & \frac{1-\varepsilon}{2} \end{pmatrix}. \tag{2.31}$$

This describes a particular instance of a mixed state, often referred to as a ε-polarized state, where $\varepsilon \in [0, 1]$. Here, the mixture consists of $(1+\varepsilon)/2$ pure state $|0\rangle \equiv |g\rangle$ and $(1-\varepsilon)/2$ pure state $|1\rangle \equiv |e\rangle$. The polarization ε is related to the von-Neumann entropy S such that $\varepsilon = 0$ results in the maximally mixed state, with maximal $S = \ln(2)$, and $\varepsilon = 1$ results in the pure target state $|0\rangle$ with $S = 0$. In other words, an increased polarization is equivalent to a decreased entropy, and a purer state. The goal of algorithmic cooling is to redistribute entropy among a set of qubits so that the target subset has lower entropy, and therefore higher polarization, while the remaining qubits have higher entropy.

To illustrate the mechanism behind reversible algorithmic cooling, we consider a simple example with two qubits A and B, both ε-polarized. The joint state $\hat{\rho}_J$ can then be written

$$\hat{\rho}_J = \hat{\rho}_A \otimes \hat{\rho}_B = \hat{\rho}(\varepsilon) \otimes \hat{\rho}(\varepsilon). \tag{2.32}$$

Reversible algorithmic cooling then consists of two sub-routines: *boosting* and *purification*. The boosting is represented as the unitary map $(\hat{a}, \hat{b}) \mapsto (\hat{a} \oplus \hat{b}, \hat{b}) = (\hat{a}', \hat{b}')$, which can be understood as a CNOT operation with control $\hat{b}$ and target $\hat{a}$, see Figure 2.6. For our example, applying this to the joint state $\hat{\rho}_J$, with $\hat{a} = \hat{\rho}_A$ and $\hat{b} = \hat{\rho}_B$, and extracting the reduced state for qubit A, $\hat{\rho}'_A$, we find

$$\hat{\rho}'_A = \hat{\rho}(\varepsilon = \varepsilon' = \varepsilon^2), \tag{2.33}$$

such that it is now polarized with $\varepsilon' = \varepsilon^2$. As $\varepsilon^2 < \varepsilon$ for $\varepsilon \in [0, 1]$, this qubit has increased entropy after the boosting, and is therefore termed a "warm" qubit moving forward. Due to the conditional nature of the boosting step (i.e., the CNOT), the polarization ε_B will depend on the resulting state of $\hat{\rho}'_A$. It is rather straightforward to show that this will be $\varepsilon_B = 2\varepsilon/(1+\varepsilon^2) > \varepsilon$ if $A' = 0$, and $\varepsilon_B = 0$ if $A' = 1$, with probabilities $P_{A'=0} = (1+\varepsilon^2)/2$ and $P_{A'=1} = (1-\varepsilon^2)/2$. Put differently, outcome $A' = 1$ will put qubit B in the maximally mixed state, making it "hot", while $A' = 0$ will decrease the entropy of B, making it colder. From the resulting polarizations, one can check that the von-Neumann entropy indeed is conserved, which can be understood directly from the fact that the boosting map is unitary (meaning that it preserves the eigenvalues, and thus the total entropy, of the joint state).

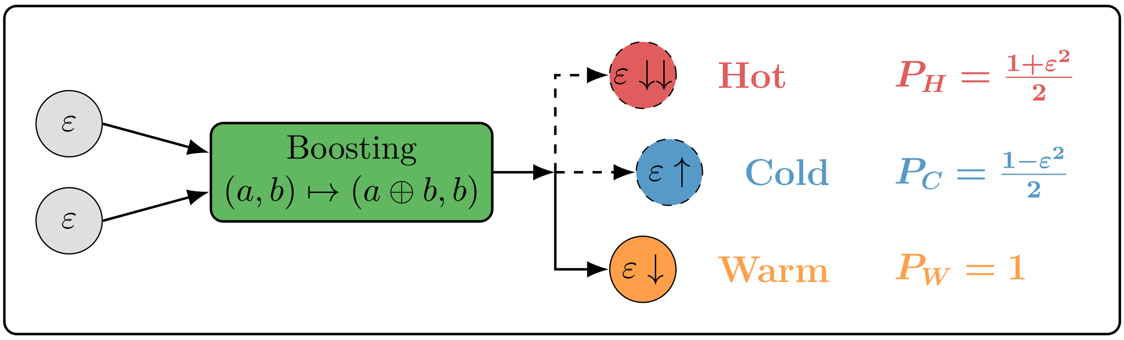

Figure 2.6: Schematic view of the boosting step in reversible algorithmic cooling. For a pair of qubits with polarization ε, the boosting results in a slightly de-polarized "warm" qubit and either a highly de-polarized "hot", or polarized "cold" qubit.

This is the main and essential part of reversible algorithmic cooling, even though the boosting step alone does not produce a set of purified qubits. Instead, the boosting serves as a primitive of the larger purification protocol. In the ideal case, the purification would just mean that we repeatedly boost cold and warm qubits, while discarding hot ones. This could be realized by ordering the qubits by their expected polarization and throwing away the "hot part" of that sequence. However, as the boosting output is a random-variable (as cold and hot qubits are produced with certain probabilities) and the operation protocol must be independent of quantum state, we cannot simply "push" a qubit left or right depending on if it is hot or cold.

The workaround to this is to instead organize the qubits after their *expected* polarization under the stochastic boosting process. In other words, the practical purification operates on blocks of qubits, rather than identifying individual copies as cold or hot. After each boosting round, the number of cold qubits fluctuates to little extent. This number is, however, sharply concentrated to its expected value, allowing us to keep the cold core of a certain block after each boost. The practical purification protocol is therefore designed as follows. Initially, the qubits are boosted pairwise and separated into cold, warm, and hot blocks using expected polarization, see Figure 2.7. From here, a controlled fraction of the warm and a safe subset of the cold qubits are kept (corresponding to the number of cold qubits guaranteed with high probability). The rest, including hot qubits and the uncertain tail of the cold sector, are discarded. At this point, the purification is split into two phases, which control the specifics of whether to discard or keep the surviving blocks.

In phase 1, the previous steps are repeatedly applied to blocks that are not already too hot or too cold. When a certain block is above a certain threshold polarization, it is termed "certified" and set aside. In phase 2, the previous steps (excluding phase 1) are applied only to certified sets. However, hot outputs are now discarded directly, together with blocks that remain warm and therefore do not cool rapidly. More specifically, phase 2 is divided into several subphases, where hot blocks are discarded during each subphase, while blocks that have remained warm too often are discarded at the end of each subphase. Put together, the boosting and purification steps are repeated until the desired number of purified qubits is produced.

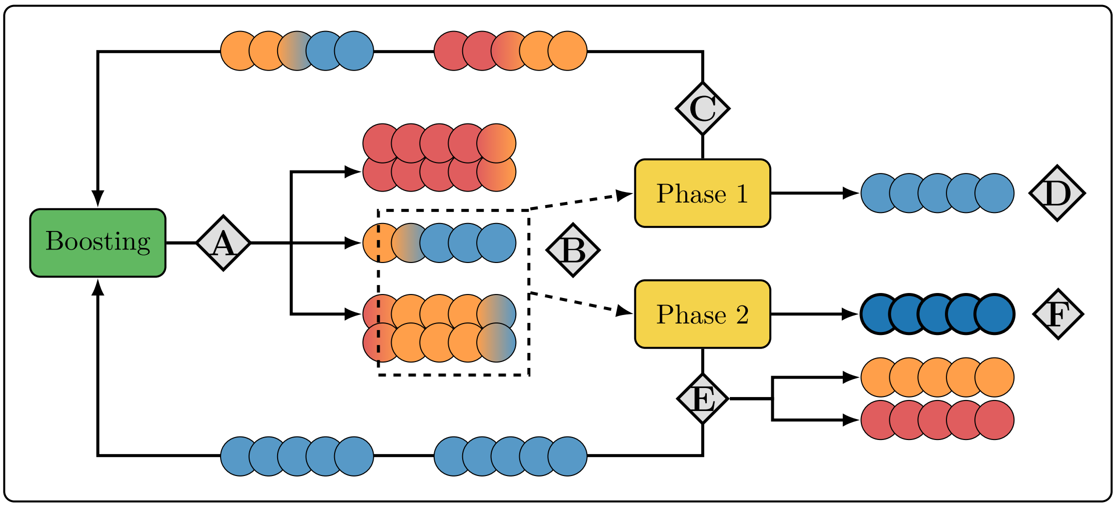

Figure 2.7: Schematic overview of the purification in reversible algorithmic cooling. **(A)** Firstly, qubits are pairwise boosted and sorted into hot, warm, and cold blocks after expected polarization. **(B)** From here, controlled fractions of the warm and cold blocks are passed to the next stage, after which the protocol splits into two phases. **(C)** During phase 1, step A and B are repeated on blocks that are either not too hot or too cold until their expected polarization is below some threshold value, and are set aside as "certified" blocks for phase 2 **(D)**. **(E)** Phase 2 then repeats steps **A** and **B** on certified blocks, while discarding blocks that are hot or do not cool quickly enough. **(F)** By repeating the whole algorithmic cooling protocol, one ideally ends up with a smaller set of purified qubits within the larger initial set.

Unfortunately, the purification also demonstrates the bottleneck of reversible algorithmic cooling. Since this protocol is inevitably probabilistic, a large number of qubits must be employed to cool a subset of arbitrary size. Mathematically, this can be expressed as an upper bound on the number of purified qubits m that can be produced from a total number of qubits n with initial polarization ε_0,

$$m \leq n\left(1 - S\left(\frac{1+\varepsilon_0}{2}\right)\right) \approx n\frac{\varepsilon_0^2}{2\ln(2)}, \ \varepsilon_0 \ll 1. \tag{2.34}$$

Therefore, reversible algorithmic cooling requires a large initial qubit set to produce even a small set of purified qubits. This limitation is based on the fact that reversible algorithmic cooling preserves total entropy, meaning that it cannot create new purity. We are thus bounded by the initial purity, which prevents us from reaching arbitrarily high purity in the final ensemble. This naturally leads us to irreversible algorithmic cooling, which applies an external heat bath to beat this bound, making it more appealing for any real-world realization of algorithmic cooling.

2.4.2 Heat-Bath Algorithmic Cooling (HBAC)

To overcome the upper bound on the number of purified qubits given in Equation 2.34, irreversible algorithmic cooling (HBAC), employs an external heat bath as an “entropy-dump”, allowing for more effective cooling. This was proposed in 2001 by Boykin et al. [2], and is fundamentally based on the same principles as reversible algorithmic cooling. Specifically, it uses the same boosting principle to redistribute the entropy within the system. Contrary to regular algorithmic cooling, however, HBAC then includes a *cooling* protocol, where the thermal states of the hot qubits are reset using the heat bath.

The heat bath consists of partially polarized qubits, and assumes that the polarization of any qubit interacting with the bath quickly reaches the collective bath polarization. Intuitively, the heat bath thus acts a sink, where the excess entropy collected by the hot qubits is dumped into the surrounding environment. In other words, the hot qubits are turned into warm qubits again, instead of disregarding them as in reversible algorithmic cooling. The purification of HBAC is then similar to that of regular algorithmic cooling, where boosting and cooling protocols are repeatedly applied to a set of qubits. Most importantly, the HBAC set-up pushes the upper bound for the total number of purified qubits achievable, as the cooling step allows us to re-use the hot qubits.

2.4.2.1 Extended Heat-Bath Algorithmic Cooling

Since its introduction, several new and improved versions of HBAC have been designed. In this thesis, we focus on the *extended heat-bath algorithmic cooling* variant proposed by Álhambra et al. [3]. This version exploits multilevel transmons, whose additional energy levels provide more pathways for entropy transfer to enhance the entropy redistribution and the cooling effect in the HBAC protocol. Theoretically, the algorithm works for d-dimensional systems (i.e., transmons with arbitrary many energy levels), but for the purpose of this thesis we will only consider qubits as target systems. Another difference between regular HBAC and extended HBAC is that the latter in general does not require any additional auxiliary systems, saving significant computational cost for preparing and controlling such systems. The authors also show, as a consequence of leveraging multilevel systems, that even the cooling (reset) step is not a hard requirement to achieve optimal cooling.

Independently of the system dimension, however, the extended HBAC protocol boils down to a three-step process. Firstly, to achieve the most efficient entropy transfer, the target system is prepared in its *maximally active state*. Physically, this can be understood as a way of re-arranging the energy within the system such that it becomes extractable. In the case of a single target qubit, this corresponds to swapping the ground and excited state population using a so-called π-pulse. Next, the cooling part occurs through the β-$SWAP$ operator. For a single target qubit, this could be realized from the interaction between the qubit and a single bosonic mode, for instance a multilevel transmon. That operator would then be given by

$$\hat{U}_\beta = |g,0\rangle\langle g,0| + \sum_{n=1}^{\infty} |g,n\rangle\langle e,n-1| + |e,n-1\rangle\langle g,n|, \tag{2.35}$$

where $|Q,B\rangle = |Q\rangle \otimes |B\rangle$, with $Q = g,e$ and $B = 0,1,2,\ldots$ are basis state vectors of the composite qubit-bosonic-mode system. The left panel of Figure 2.8 shows the effect one round of applying $\hat{U}_\beta$ to the maximally active state of the target qubit in the case of an infinite-level bosonic mode. Here, the bosonic mode would act as an infinite "entropy well", where entropy can be stored without saturation and transported away from the target system over successive cycles, efficiently pushing the qubit population in the opposite direction, indicated by the dashed and dotted arrows in Figure 2.8. In this case, the re-thermalization is thus not mandatory, as the infinite mode can be reused over consecutive cooling cycles, acting as an unbounded entropy sink that allows the qubit to iteratively approach its ground state.

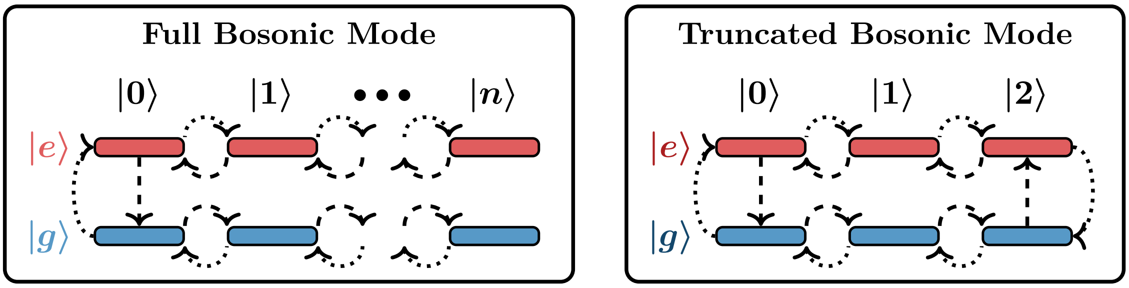

Figure 2.8: Schematic view of the net entropy (dotted) and population (dashed) flow after applying the first two operations of the extended HBAC protocol — the qubit excitation and the β-SWAP — in the single-qubit target example system. When all levels of the bosonic mode are accessible (left panel), each round of these operations successively pushes population towards the ground state of the qubit, by using the mode as an infinite "entropy well". In real life, only a few levels are accessible (right panel), causing the population to oscillate between $|g\rangle$ and $|e\rangle$, and never converge to the ground state. Figure adapted from [3].

However, this thesis explores the experimental implementation of extended HBAC, which unfortunately makes our lives harder than the ideal, theoretical version suggests. In practice, the most important bottleneck for the experimental implementation of extended HBAC is that we cannot employ infinite energy levels of the bosonic mode. As illustrated by Figure 2.8, this will cause population (and entropy) to circle around within the system, and never converge to the ground state. Luckily, there is a workaround to this problem. By re-thermalizing the bosonic mode after each cooling iteration, the accumulated entropy can be dissipated into an external environment, restoring the mode to its thermal state and recovering its cooling capacity for the next cycle. This can for example be realized by coupling the mode to a resonator that relaxes it to the surrounding thermal environment of the resonator. Figure 2.9 illustrates an experimentally feasible workflow for the extended HBAC protocol applied to a single-qubit target system, building on the above.

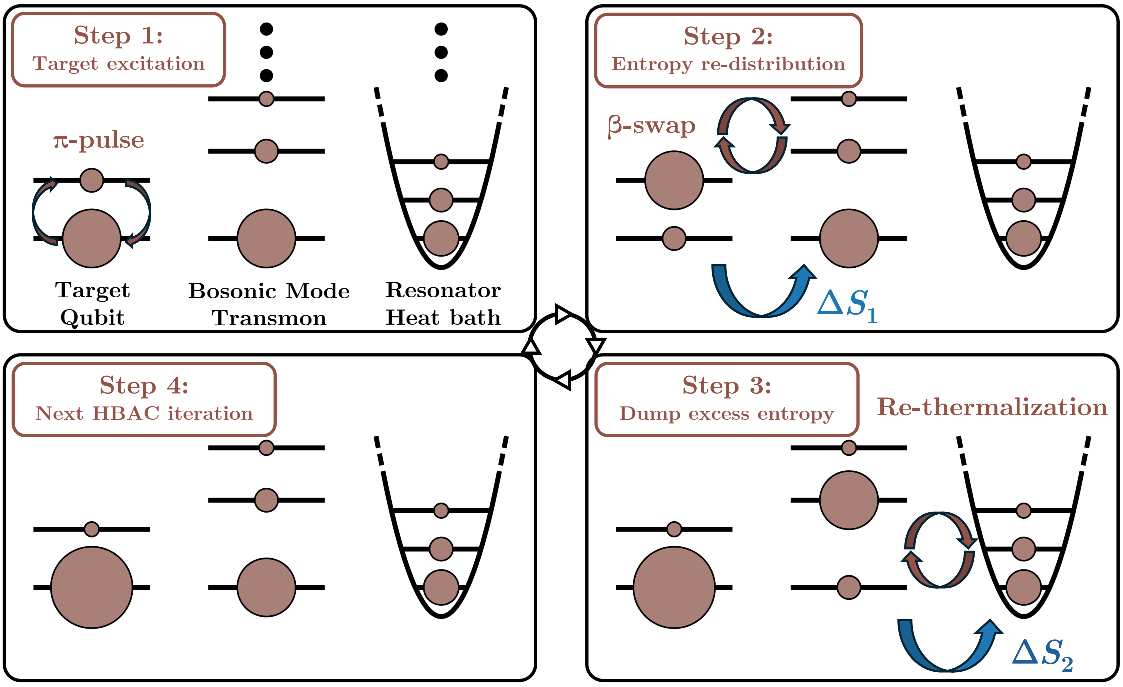

Figure 2.9: Schematic picture showing an experimentally feasible extended HBAC principle for a single-qubit target system. First, the qubit is excited to achieve the maximally active state by swapping the ground and excited state populations. Secondly, the β-SWAP exchanges population between the target qubit and bosonic mode, removing entropy from and thus cooling the qubit, indicated by the blue arrows. Finally, the bosonic mode is re-thermalized by transferring the excess entropy to the external heat bath, preparing for the next cooling iteration.

Even though the re-thermalization theoretically will work equally well as the perfect bosonic mode setup, there is a clear disadvantage with re-thermalizing the system, which in this case — as in many others — has to do with time. When performing the extended HBAC protocol, our greatest enemy is the relaxation rate of the target qubit, or equivalently its T_1^q. If this is shorter than the execution time of a single cooling round, the qubit will relax back to its initial thermal state, and the cooling effect will be negligible. In the case of not re-thermalizing the bosonic mode, this is avoided if the β-SWAP-time τ_β is much smaller than T_1^q, i.e., $\tau_\beta \ll T_1^q$. However, if we add the re-thermalization, we must instead make sure that

$$\tau_\beta + \tau_{\mathrm{R}} \ll T_1^q, \tag{2.36}$$

where τ_{R} is the execution time of the re-thermalization. By adding this extra time dimension to the protocol, the importance of a reliable target qubit T_1^q increases. Of course, there are other disadvantages regarding the need of implementing and controlling the re-thermalization, but this is the most fundamental one, as it directly limits the cooling performance of the protocol. Thus, to achieve optimal cooling, we need to make sure that the β-SWAP is as fast as possible, while also keeping the re-thermalization time at a minimum.

3

Methods

It is now time for us to leave (but not forget) the theoretical models from the last chapter to acknowledge the actual implementation of extended HBAC in a superconducting quantum circuit. Below, we start by characterizing the experimental setup, including the qubit device and cryogenic set-up. After that, we split the implementation into two parts. The first part covers the realization of the β-SWAP operator $\hat{U}_\beta$, mathematically defined in Equation 2.35. Following the extended HBAC protocol structure from start to finish, the second part then naturally involves the implementation of the re-thermalization of the bosonic mode. Finally, we describe how these two parts are combined to form the complete protocol.

3.1 Experimental Setup

The most essential part of an experimental project is arguably the experimental setup. This is not an exception in this thesis, where the qubit device and cryogenic wiring is crucial for realizing the extended HBAC protocol. Below, these parts of the methodology is outlined in detail, laying the foundation for the actual implementation, as described in the following sections.

3.1.1 Cryostat Configuration

The most important part of circuit QED experiments is undeniably the dilution refrigerator, also known as the *cryostat*. This allows us to reach extremely low temperatures, which as we know is foundational for achieving superconductivity and thus realizing a reliable platform for circuit QED research. In addition to superconductivity, the low temperature is also crucial for qubit lifetime and thermal noise reduction. This thesis uses a BlueFors LD Dilution Refrigerator System, operated near 70 mK. Details about the functionality and operation of this particular cryostat can be found online [37]. In short, however, a cryostat uses a mixture of the helium isotopes He^3 and He^4 to achieve the low temperatures. The mixture is circulated through a series of stages with decreasing temperature, ultimately reaching the base temperature at the mixing chamber stage where the qubit device is located.

Figure 3.1 shows the wiring diagram inside and outside of the cryostat. The setup consists of two inputs (qubit and modulation lines) and one output, where the former is used to control the qubits and the latter for readout purposes. Each input has a number of attenuators at each temperature stage to remove thermal noise whilst the surrounding temperature decreases, ensuring appropriate signal energy scales when it reaches the qubit device. Contrary to the input lines, the readout line instead has a number of amplifiers, used to convert the attenuated signal from the cryogenic chip to a level where it can be measured and analyzed at room temperature. The DC block, isolator, and circulator all make sure that no signal enters the qubit device from the output line. In addition to the input and output, the setup includes a DC breakout box, used to apply a current that tunes the frequency of the coupler. This is combined with the modulation line signal through a bias tee, an electrical component that allows DC and radio-frequency (RF) signals to share the same physical line while keeping the two frequency components separated.

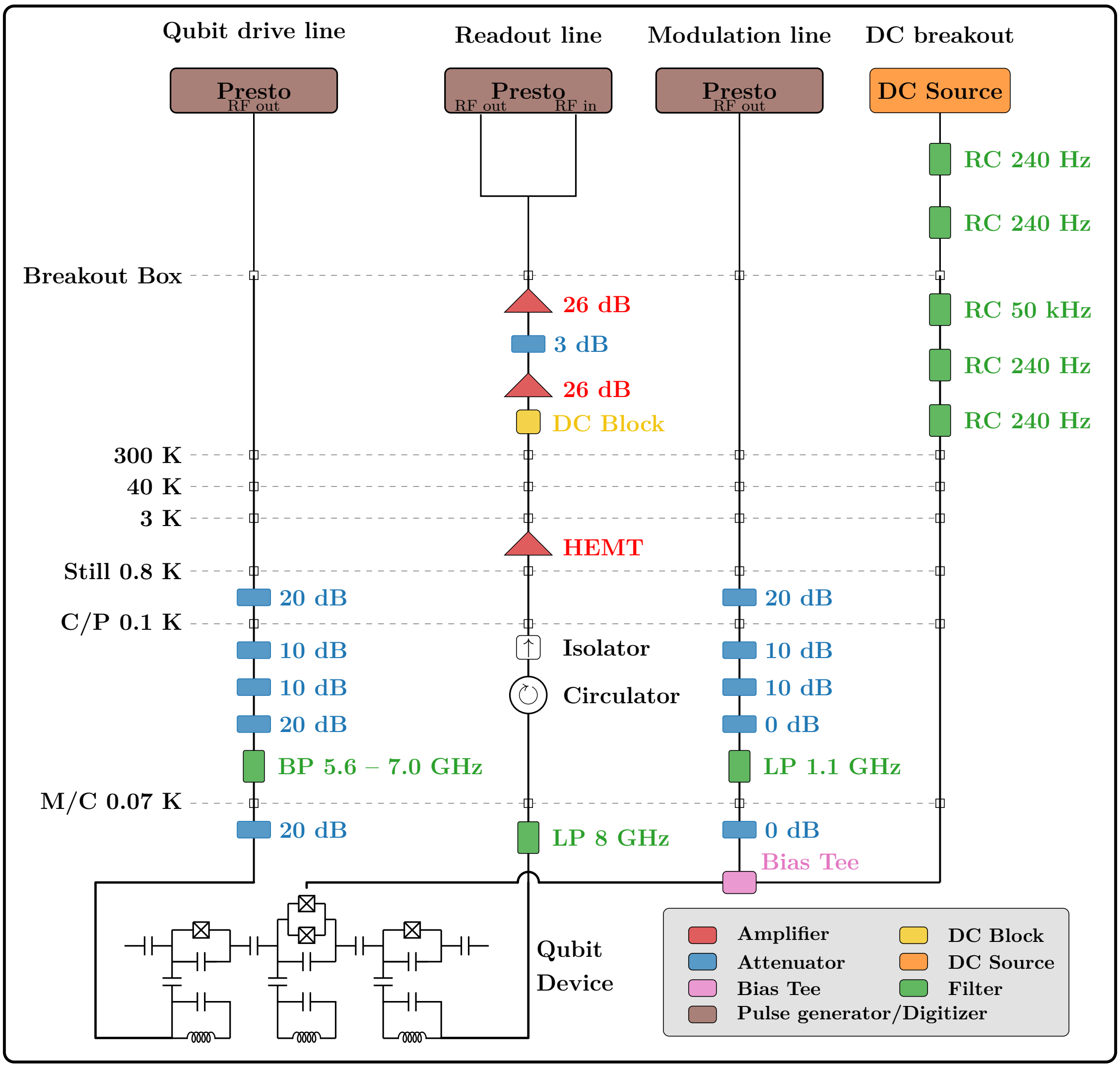

Figure 3.1: Simplified scheme showing the wiring diagram used in the project. The dashed horizontal lines correspond to different temperatures within the cryostat. For a more detailed figure and description of the qubit device, we refer to Section 3.1.2.

Using an arbitrary waveform generator, the RF signals could be generated with controllable amplitude, phase, and frequency. This is especially useful for circuit QED experiments, where the customization of shaped pulses is crucial for qubit control. Particularly, the waveform generator is a 16-output-version of the Presto device, which functionality can be found online [38], [39]. In total, we use five Presto output ports and one input port. For the latter port, the Presto device digitizes the returned signal such that the measurement response can be represented as complex-valued I/Q data. Among the output ports, two are used to drive the qubits, two more to probe their respective resonator, and the last one to drive the modulation line. To combine the qubit and resonator outputs to the chip input line, we use power splitters. Furthermore, to remove spurious tones, several room-temperature low- and high-pass filters are applied to the Presto input and output.

3.1.2 The Device

Figure 3.2 shows the device used in this thesis, consisting of a tunable transmon between two fixed-frequency qubits. The intended application of the tunable transmon is to tune the coupling strength between the qubits. Therefore, it is commonly referred to as a *coupler qubit* (CQ). In this thesis, we only employ one of the qubits, the target qubit (TQ), together with the coupler to implement the extended HBAC protocol. All qubits are capacitively coupled and have their own resonator used for readout. Notably, this chip was not custom-made for extended HBAC, but its general structure shows that a successful implementation would not require a specifically designed device, strengthening the case for the general applicability of HBAC in superconducting circuits. Next, we describe the device characterization, which forms the foundation for implementing the extended HBAC protocol.

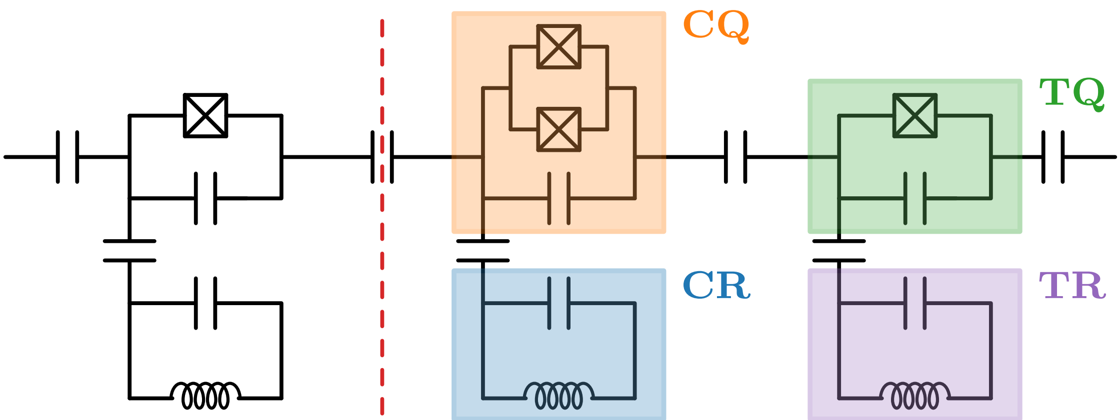

Figure 3.2: Schematic view of the project device, consisting of a tunable coupler qubit (CQ) and two fixed-frequency transmons, one of which acts as the target qubit (TQ) for the extended HBAC protocol. Each qubit also has its own resonator (R) used for readout purposes. The left transmon qubit was not used within the scope of this project, as indicated by the dashed line.

3.2 System Characterization

Before starting the extended HBAC implementation in the device, it is imperative to understand and classify its foundational properties. This is done by characterizing the qubits and resonators, as well as the combined system. In the context of extended HBAC, relevant parameters for the qubits include their frequencies ω_q, anharmonicities α, and relaxation and coherence times T_1 and T_2. For the resonators, we are interested in their frequencies ω_r and decay rates κ. Finally, for the combined system, we need to know the detuning between the target and coupler qubits Δ_{qc} and between the coupler and its resonator Δ_{c_rc}, as well as the coupling strengths g_{qc} and g_{c_rc}. We park the coupler qubit at a frequency of 6.00 GHz using a bias current of 818.16 µA. Since the coupler sweet spot is very close to its resonator, we chose another operation point as it otherwise would relax too quickly, preventing an effective β-SWAP. The chosen parking spot allows a fast re-thermalization while maintaining a rapid and reliable β-SWAP. The measured values for these parameters at this particular parking spot are summarized in Table 3.1 below.

Table 3.1: Measured qubit and resonator parameters for the relevant device modes.

Parameter [Unit]	**Symbol**	**Target**	**Coupler**
QUBIT PARAMETERS			
Frequency [GHz]	$\omega_q/2\pi$	5.26	6.00
Anharmonicity [MHz]	$\alpha/2\pi$	–212.2	–68.19
Relaxation time [µs]	T_1	37	15
Coherence time [µs]	T_2	11	1.7
Dispersive shift [kHz]	$\chi/2\pi$	697.5	50
RESONATOR PARAMETERS			
Frequency [GHz]	$\omega_r/2\pi$	6.74	7.82
Decay rate [kHz]	$\kappa/2\pi$	765.8	615.6
COMBINED-SYSTEM PARAMETERS			
Target-coupler detuning [GHz]	$\Delta_{qc}/2\pi$	0.74	
Coupler-resonator detuning [GHz]	$\Delta_{c_rc}/2\pi$	1.82	
Target-coupler coupling [MHz]	$g_{qc}/2\pi$	42	
Coupler-resonator coupling [MHz]	$g_{c_rc}/2\pi$	50	

Regarding the parameter acquisition techniques, we employ standard circuit QED methods whilst working in the dispersive regime. For the resonator frequencies and decay rates, that is one-tone spectroscopy, in which a weak probe tone is swept across the resonator while measuring the transmitted signal. At resonance, the response signal shows a characteristic amplitude and phase response, from which the frequency and decay rate can be determined. More specifically, we use the framework provided by Probst et al. to extract ω_r and κ from the data [40].

After the resonator frequency of a qubit has been determined, the qubit frequency and anharmonicity can be found similarly using two-tone spectroscopy. Here, one tone is parked at the resonator whilst another tone sweeps across the qubit frequency. Since we are working in the dispersive regime, the resonator frequency will shift when the qubit frequency is hit, typically exhibited as a dip or a peak in the transmitted signal. In practice, the qubit drive is performed in short pulses of 100 µs, followed by a readout pulse. This allows us to avoid frequency shifts from the qubit-resonator coupling during the measurement, yielding a more precise frequency estimation. Moreover, by probing the qubit with more power, the anharmonicity can be approximated by inducing the $|g\rangle \leftrightarrow |f\rangle$ transition frequency $\omega_d = \omega_{gf}/2$,

$$\alpha = \omega_{ef} - \omega_q = \omega_{gf} - 2\omega_q = 2(\omega_d - \omega_q), \tag{3.1}$$

where the factor 2 arises from the fact that this is a two-photon transition. A more general, and precise method, however, would be to excite the qubit and perform a $|e\rangle \rightarrow |f\rangle$ Ramsey experiment (see below).

Next, we find the relaxation time, coherence time, and dispersive shift χ by performing time-domain measurements. Intuitively, we measure the dispersive shift χ through one-tone spectroscopy after exciting the qubit. The T_1 time is found by preparing the qubit in the excited state $|e\rangle$ using a well-calibrated π-pulse and measuring the population decay back to the ground state $|g\rangle$ as a function of time. T_2 is measured similarly by performing a Ramsey experiment. Starting by slightly detuning the qubit frequency, the qubit is prepared in a superposition $(|g\rangle + |e\rangle)/\sqrt{2}$ through a $\pi/2$-pulse and then allowed to evolve freely as a function of time before applying another $\pi/2$-pulse. From the T_2 measurements, we can also fine tune the qubit frequency by extracting the detuning from a fit on the T_2 data and compare that to the theoretical detuning set before the experiment.

Finally, we determine the qubit-coupler and coupler-resonator coupling rates using two different methods. Firstly, we find the qubit-coupler coupling g_{qc} by letting the coupler frequency "pass" over the target qubit by sweeping the coupler current bias. This results in a so-called *avoided crossing* due to quantum hybridization, meaning that the two modes will repel each other when they are close in frequency. The coupling strength is then extracted from the size of this avoided crossing, which is given by $2g_{qc}$. On the other hand, the coupler-resonator coupling g_{c_rc} is measured by combining experiments with the analytical expression for the dispersive shift χ in the Jaynes-Cummings model, that is

$$\chi = \frac{g_{c_rc}^2 \alpha_c/\hbar}{\Delta_{c_rc}(\Delta_{c_rc} + \alpha_c/\hbar)}, \tag{3.2}$$

where Δ_{c_rc} is the detuning between the coupler and its resonator and α_c the anharmonicity of the coupler [29]. By measuring χ of the coupler resonator through one-tone spectroscopy and knowing Δ_{c_rc} and α_c from the previous characterization, g_{c_rc} could be calculated.

3.3 Experimentally Realizing Extended HBAC

The following sections describe the practical realization of the extended HBAC protocol in a superconducting circuit. We begin by clarifying the individual functionality and implementation of the β-SWAP and re-thermalization, ultimately leading to a proposal on how these can be combined to implement the whole protocol.

3.3.1 β-SWAP Operator

To implement the β-SWAP operator $\hat{U}_\beta$ defined in Equation 2.35, we employ the same method demonstrated by Reagor et al. for a tunable transmon (the coupler in our case), and fixed-frequency transmon (our target qubit) [35]. The theory behind this is described in Section 2.3.3.2. In this thesis, we focus on the first two transitions of $\hat{U}_\beta$, i.e., $|g1\rangle \leftrightarrow |e0\rangle$, denoted $\hat{U}_\beta^{(1)}$, and $|g2\rangle \leftrightarrow |e1\rangle$, denoted $\hat{U}_\beta^{(2)}$. Here, we use the notation $|QC\rangle$ for the target qubit (Q) and coupler (C), which acts as our bosonic mode. These terms also appear in the interaction Hamiltonian modeling a qubit coupled to a tunable transmon in Equation 2.28, with the corresponding effective coupling strength pre-factors. Physically, this means that we can induce energy transitions between these states by probing the coupler at given frequencies. In particular, $\hat{U}_\beta^{(1)}$ is implemented by probing the qubit at the modulation frequency $\omega_m^{(\beta_1)} = \pm\Delta_{qc} = \pm(\omega_q - \omega_c)$, where ω_q and ω_c are the frequencies of the target and coupler, respectively. Similarly, $\hat{U}_\beta^{(2)}$ is implemented by probing the qubit at $\omega_m^{(\beta_2)} = \pm(\Delta_{qc} - \alpha_c)$, where α_c is the anharmonicity of the coupler.

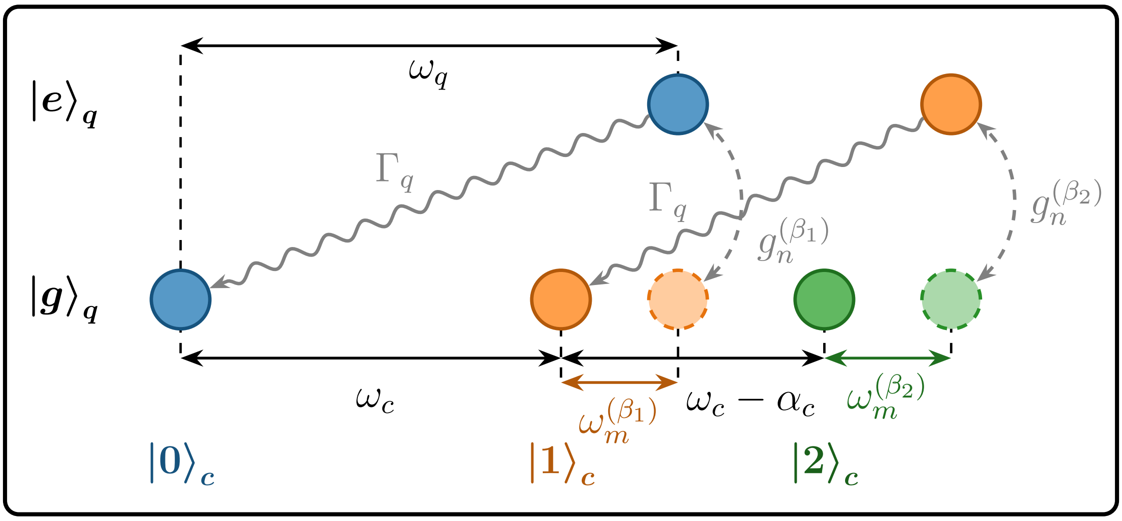

Figure 3.3: Schematic figure of the Jaynes-Cummings diagram for the combined target-coupler system, illustrating the β-SWAP realization. The states $|g\rangle_q$, $|e\rangle_q$, and $|0\rangle_c$, $|1\rangle_c$, $|2\rangle_c$ are the lowest energy states for the target and coupler, respectively. By modulating the coupler at frequencies $\omega_m^{(\beta_1)}$ and $\omega_m^{(\beta_2)}$, an energy exchange between the target and coupler is achieved, realizing the first two transitions of $\hat{U}_\beta$.

In practice, we target and calibrate these transitions individually by sweeping the pulse length τ_β and ω_m for each transition. This results in a Rabi-Chevron pattern, showing oscillations between the involved states as a function of τ_β and ω_m. From this, the optimal frequency $\omega_{m,\star}$ is found by fitting the Rabi-oscillation frequency of each ω_m to a sinusoid, resulting in a quadratic function with its minimum at $\omega_{m,\star}$. Finally, the oscillations for $\omega_{m,\star}$ are used to find the optimal pulse length $\tau_{\beta,\star}$, i.e., the point of the first extremum, corresponding to a full population transfer between the two involved states. In theory, the initial state of this experiment should not matter, since the transition goes both ways, according to the Hamiltonian in Equation 2.28. Therefore, we perform the experiments using $|g1\rangle$ and $|g2\rangle$ as initial states. For $\hat{U}_\beta^{(2)}$ in particular, this is more practical than starting in $|e1\rangle$, where crosstalk, i.e., target frequency shifts from coupler excitation, will be more prominent.

This naturally translates to the next challenge. According to the definition of the β-SWAP operator, all involved terms should happen *simultaneously* and *at the same rate*. The solution to the latter is rather straightforward. By tuning the modulation amplitude of each term, τ_β can be calibrated to the same value for both terms. Theoretically, $\hat{U}_\beta^{(2)}$ is $\sqrt{2}$ times faster than $\hat{U}_\beta^{(1)}$ (courtesy of the Hamiltonian $\sqrt{2}$ pre-factor). Thus, we drive the $\hat{U}_\beta^{(1)}$ about $\sqrt{2}$ times stronger. The simultaneous implementation, on the other hand, is trickier. However, since the involved states are orthogonal, they should not interfere with each other. Thus, we apply the two ω_m sequentially without affecting the dynamics of the other, saving us time when it comes to calibrating them simultaneously. This would be harder as it would induce ac-Stark shifts in ω_m and other obstructing dynamics.

3.3.2 Re-thermalization of the Bosonic Mode

The re-thermalization of the bosonic mode, or the coupler qubit in our case, is implemented similarly to the β-SWAP by realizing an energy exchange between the coupler and its resonator. The theory behind this kind of interaction was described earlier in Section 2.3.3.3. After the β-SWAP has been applied to the target-coupler system, the coupler $|1\rangle_c$ and $|2\rangle_c$ states will hold excess entropy extracted from the target qubit, and must therefore be reset before the next cooling round to avoid entropy saturation, as described earlier.

Depending on if we employ only $\hat{U}_\beta^{(1)}$, or both $\hat{U}_\beta^{(1)}$ and $\hat{U}_\beta^{(2)}$, either $|1\rangle_c$ or both $|1\rangle_c$ and $|2\rangle_c$ will hold the excess entropy. In the first case, we only need to reset $|1\rangle_c$, which in general is more straightforward than resetting both $|1\rangle_c$ and $|2\rangle_c$. In both cases, however, we employ the method outlined by Zhou et al. [36]. Following their recipe for resetting only $|1\rangle_c$, we constrain our system subspace to that spanned by $\{|01\rangle, |10\rangle\}$, where we use the notation $|RC\rangle$ for the resonator (R) and coupler (C). This is justified when the modulation frequency ω_m of the total system Hamiltonian in Equation 2.30 is chosen such that $n\omega_m \simeq \pm\Delta_{rt}$, which suppresses higher order transitions. When also including the photon loss (decay) of the coupler resonator, the effective Hamiltonian for this truncated system can be written

$$\hat{H}_R = \begin{pmatrix} 0 & |g_n^R|e^{i\beta_n} \\ |g_n^R|e^{-i\beta_n} & -i\kappa_{c_r}/2 \end{pmatrix}. \tag{3.3}$$

Here, g_n^R and β_n are the effective coupling strengths and interaction phases of the total system Hamiltonian, and κ_{c_r} is the coupler resonator decay rate. From this, the reset rate, specifying the overall reset speed, is obtained from the imaginary parts of the eigenvalues of $\hat{H}_R$, which determine the decay rates of the states involved. Depending on the modulation amplitude, three decay regimes are possible. For small amplitudes, specifically $|g_n^R| < \kappa_{c_r}/4$, the $|1\rangle_c$ decay will be similar to a regular T_1, where Γ increases with $|g_n^R|$. For our goal, however, we want to be in the *underdamped*, or preferably the *critically damped* regime, where Γ will have its maximum value $\Gamma = \kappa_{c_r}/2$, enabling a fast reset. The former is achieved when $|g_n^R| = \kappa_{c_r}/4$, and the latter when $|g_n^R| > \kappa_{c_r}/4$.

In practice, since the resonance criteria in the total system Hamiltonian reads $n\omega_m = \pm\Delta_{rt}$, several sidebands n realize the energy exchange. We will, however, only need one of these to reset the coupler, as this alone will induce the $|01\rangle \leftrightarrow |10\rangle$ transition, in analogue to our β-SWAP implementation, see the blue-orange interaction in Figure 3.4. By sweeping the modulation frequency $\omega_m^{(R_1)}$ and amplitude, where the latter controls the effective coupling strengths g_n, the different sidebands is found, enabling us to find the optimal frequency $\omega_{m,\star}^{(R_1)}$ and amplitude that realizes the critically damped regime. Finally, we find the optimal reset time $\tau_{\mathrm{R},\star}$ by sweeping the pulse duration for the optimal frequency and amplitude.

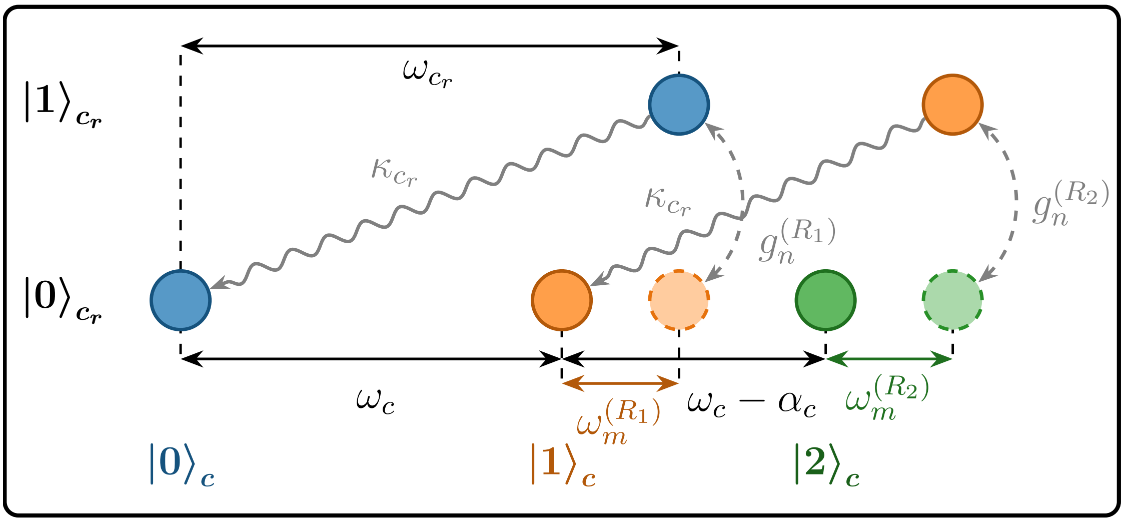

Figure 3.4: Schematic figure of the Jaynes-Cummings diagram for the combined coupler-resonator-coupler system, illustrating the idea behind the parametric reset of the coupler qubit. The states $|0\rangle_{c_r}$, $|1\rangle_{c_r}$, and $|0\rangle_c$, $|1\rangle_c$, $|2\rangle_c$ are the lowest energy states for the resonator and coupler, respectively. The curly arrows denote the resonator decay at rate κ_{c_r}. By modulating the coupler at frequencies $\omega_m^{(R_1)}$ and $\omega_m^{(R_2)}$, an energy exchange between the coupler and resonator is achieved, ultimately realizing the coupler reset through the resonator decay. Figure adapted from [36].

For resetting both $|1\rangle_c$ and $|2\rangle_c$, Zhou et al. propose a simultaneous reset by sending two simultaneous parametric modulation drives to the coupler, see Figure 3.4. These will induce energy exchange between $|01\rangle \leftrightarrow |10\rangle$ and $|02\rangle \leftrightarrow |11\rangle$, as depicted by the dashed circles above. As a result, the $|1\rangle_c$ and $|2\rangle_c$ states of the coupler will be reset via the resonator, which decays with rate κ_{c_r} according to the curly arrows. Similarly to the β-SWAP, the modulation frequencies that activate these transitions can be derived from the interaction Hamiltonian in Equation 2.30, that is $\omega_m^{(R_1)} = \pm\Delta_{c_rc} = \pm(\omega_{c_r} - \omega_c)$ for $|01\rangle \leftrightarrow |10\rangle$ and $\omega_m^{(R_2)} = \pm(\Delta_{c_rc} - \alpha_c)$ for $|02\rangle \leftrightarrow |11\rangle$, where ω_{c_r} is the coupler resonator frequency.

When sweeping both $\omega_m^{(R_1)}$ and $\omega_m^{(R_2)}$, the effective frequency will be composed of four major components, i.e., $\omega_m^{(R_1)}$, $\omega_m^{(R_2)}$, and $(\omega_m^{(R_1)} \pm \omega_m^{(R_2)})/2$. Thus, we will have several resonance regions where the transitions occur, in particular where $\omega_m^{(R_1,R_2)} = \pm\Delta_{c_rc}$, $\omega_m^{(R_1,R_2)} = \pm(\Delta_{c_rc} - \alpha_c)$, $(\omega_m^{(R_1)} \pm \omega_m^{(R_2)})/2 = \pm(\Delta_{c_rc})$, and $(\omega_m^{(R_1)} \pm \omega_m^{(R_2)})/2 = \pm(\Delta_{c_rc} - \alpha_c)$. To realize the simultaneous reset, however, we are only interested in the region where the resonance conditions for both transitions happen at the same time. This will arise when two frequency components involve the resonance conditions for both transitions, for instance when $\omega_m^{(R_1)} = \pm\Delta_{c_rc}$ and $(\omega_m^{(R_1)} \pm \omega_m^{(R_2)})/2 = \pm(\Delta_{c_rc} - \alpha_c)$. By sweeping $\omega_m^{(R_1)}$ and $\omega_m^{(R_2)}$, the optimal frequencies $\omega_{m,\star}^{(R_1)}$ and $\omega_{m,\star}^{(R_2)}$ are found. Finally, the optimal reset time $\tau_{\mathrm{R},\star}$ is found as the point where the excited state population has reached its minimum at a chosen modulation amplitude for the optimal modulation frequencies.

3.3.3 Extended HBAC Implementation

We are now ready to implement the complete extended HBAC protocol. This starts by exciting the target qubit by probing it with a π-pulse, see Figure 3.5, which is the only component of this algorithm that we have not commented on yet. It is, however, trivial to calibrate by sweeping the amplitude of a pulse probed at the calibrated $|g\rangle_q \rightarrow |e\rangle_q$ frequency. The π-pulse amplitude will then appear as the first extremum point, corresponding to a full $|g\rangle_q \rightarrow |e\rangle_q$ transfer. Next, we apply the β-SWAP operators $\hat{U}_\beta^{(1)}$ and $\hat{U}_\beta^{(2)}$ sequentially, before resetting the thermal state of the coupler qubit. Depending on if we use both $\hat{U}_\beta^{(1)}$ and $\hat{U}_\beta^{(2)}$, or only $\hat{U}_\beta^{(1)}$, the re-thermalization will require either one or two pulses. Finally, after repeating the steps above over N rounds, we measure the thermal population of the target qubit, as described in Section 3.4.2.

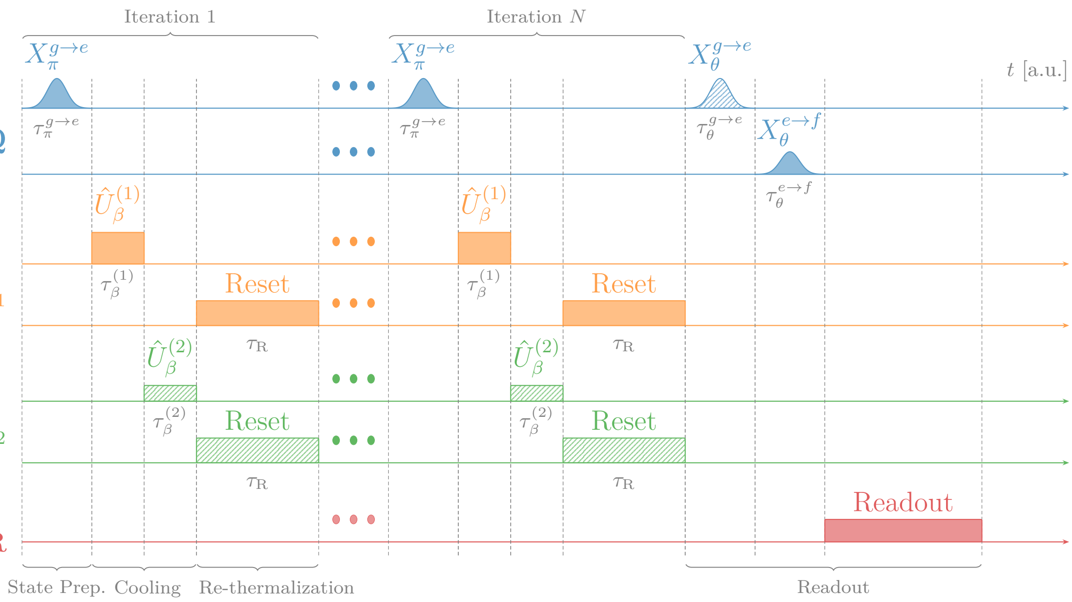

Figure 3.5: Pulse diagram for realizing extended HBAC in a superconducting circuit. Each cooling cycle consists of a target excitation, followed by a β-SWAP and a reset of the coupler. This is then repeated over N cycles before the readout.

3.4 Readout and Data Analysis

One part of an experiment procedure that is often overseen or taken for granted is data collection and analysis. However, this is not something to be taken lightly, and it can more often than not decide the quality of the results. This is particularly true in the context of circuit QED, where the readout can significantly impact the fidelity of the measurements. In general, as we perform our experiments using superconducting circuits, the response from a certain operation (pulse sequence) on our qubits is represented by an RF signal with a certain amplitude and phase. In practice, this signal is measured as a voltage response at the cryostat output, which is then digitized into a complex number. The amplitude and phase of this number are then used to infer the state of the qubits, serving as the basis for the data analysis. When it comes to the exact readout and analysis method, we use different approaches depending on the experiment, as described below.

3.4.1 Averaged Readout

For the β-SWAP and coupler reset, we employ averaged readout. By repeatedly preparing the same state, we calibrate the response for that state by averaging the measured data. This is done for all relevant states of an experiment, allowing us to create a mapping between the measured complex numbers and the corresponding qubit states. One reason why this is preferred is due to the inevitable fact that our target and coupler qubit are physically coupled, so that one operation will shift the response for the other. Average readout then lets us treat the target-coupler system as composite by calibrating the readout response for all relevant states.

For the β-SWAP implementation, we calibrate the response for the $|g0\rangle$, $|g1\rangle$, $|e0\rangle$, and $|e1\rangle$ states. The obtained complex data was then rotated in the complex plane to align the involved states with the real axis, which is a common technique used to improve the readout fidelity. Finally, the population of each state is found by projecting the measured data onto the real axis, using the calibrated mapping to infer the state populations. For example, if a measured complex number from the $\hat{U}_\beta^{(1)}$ operation ends up in between the calibrated $|g1\rangle$ and $|e0\rangle$ responses, we infer that the population of these two states is 50%. However, since this measurement only use the target resonator, the composite system state cannot be inferred, so that the actual interpretation would be to 50% of $|g\rangle_q$ and $|e\rangle_q$.

Similarly, we start by calibrating the coupler resonator response for the $|00\rangle$, $|01\rangle$, and $|02\rangle$ states for the re-thermalization. When only resetting $|1\rangle_c$, we employ the same method as for the β-SWAP. When resetting both $|1\rangle_c$ and $|2\rangle_c$, however, we must consider the fact that all three states are involved in the reset, so that we could not simply project onto the real axis. Instead, we find the respective state population by numerically solving the linear system of equations given by

$$\begin{pmatrix} \mathrm{Re}(S_{00}) & \mathrm{Re}(S_{01}) & \mathrm{Re}(S_{02}) \\ \mathrm{Im}(S_{00}) & \mathrm{Im}(S_{01}) & \mathrm{Im}(S_{02}) \\ 1 & 1 & 1 \end{pmatrix} \begin{pmatrix} P_{0_c} \\ P_{1_c} \\ P_{2_c} \end{pmatrix} = \begin{pmatrix} \mathrm{Re}(S) \\ \mathrm{Im}(S) \\ 1 \end{pmatrix}. \tag{3.4}$$

Here, P_{i_c} is the population of coupler state i, S_{0i} the calibrated response for each state, and S the measured signal. This approach ensures that all involved states are considered, while maintaining the normalization condition $\sum_i P_{i_c} = 1$.

3.4.2 Thermal Populations Measurements

As we know, the ultimate goal of the extended HBAC protocol is to cool the target qubit. In the realm of superconducting circuits, making a qubit colder is equivalent to reducing its thermal population, theoretically described by the expression in Equation 2.12. In practice, the thermal population is a fancy way of referring to the excited state population of the qubit. Therefore, the natural way of evaluating the performance of our extended HBAC implementation is by measuring the thermal population of the target qubit. However, since this population is typically very low, on the order of a few percent, it can be challenging to measure it with high precision.

To overcome this, we employ the same method as Aamir et al., who measured thermal populations as low as 10^{-4} [20]. Simply put, they propose to use standard Rabi-oscillation measurements for two different state preparations, see Figure 3.6. Firstly, the reference signal is calibrated by exciting the qubit and measuring the $|e\rangle_q \to |f\rangle_q$ Rabi-oscillations by probing the qubit with different modulation amplitudes at the $|e\rangle_q \to |f\rangle_q$ transition frequency. Since we swap the $|g\rangle_q$ and $|e\rangle_q$ states, the $|e\rangle_q$ state is almost fully populated, and the amplitude of the oscillations will be maximal, serving as a reference for the thermal population measurement.

Secondly, we perform the same Rabi-oscillation measurement, but now without the initial excitation. The amplitude of these Rabi-oscillations, referred to as the signal, is considerably smaller than the reference, and by comparing the two amplitudes, we infer the thermal population of the target qubit. In particular, the thermal population is calculated as $P_{\text{th}} = A_{\text{s}}/(A_{\text{s}}+A_{\text{ref}})$, where A_{s} and A_{ref} are the amplitudes of the Rabi-oscillations for the signal and reference measurements, respectively. To save time, we only measure the response for $\theta \in [0, 0.5]$, since the first extremum point ($\theta = 0.5$) of the oscillations corresponds to a full $|e\rangle_q \to |f\rangle_q$ transfer, which is sufficient for estimating P_{s} and P_{ref}.

Finally, to estimate the uncertainty of P_{th}, we divide the total N averages for each measurement into M batches. For each batch, we calculate the thermal population $P_{\text{th}}^{(M)}$ independently, and the reported P_{th} value is taken as the mean of the $P_{\text{th}}^{(M)}$ values. The error bars are then determined by the standard error of the mean, that is $\sigma_M/\sqrt{M}$, where σ_M is the standard deviation of the $P_{\text{th}}^{(M)}$ values.

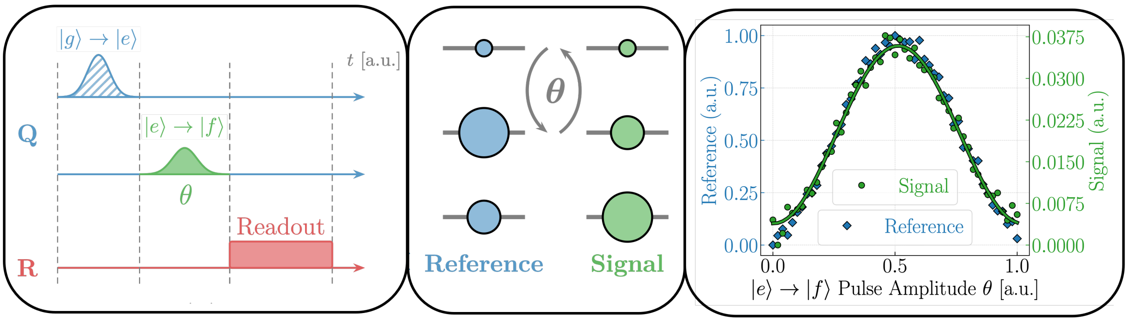

(a) **(b)** **(c)**

Figure 3.6: Schematic overview of the thermal population measurement for the target qubit. **(a)** and **(b)** By sweeping the $|e\rangle_q \to |f\rangle_q$ pulse amplitude with and without a prior $|g\rangle_q \to |e\rangle_q$ π-pulse, the reference and signal data is acquired, respectively. **(c)** The thermal population can then be estimated via the amplitudes of the resulting Rabi-oscillations. Figure adapted from [20].

4

Results

Below we present the results for the different stages of realizing extended HBAC in a superconducting circuit, starting with the implementation of the β-SWAP operator, followed by the re-thermalization of the coupler qubit. Finally, we also present the results of the full extended HBAC protocol, which combines the two previous steps in two different fashions. The results are mainly presented in the form of figures, which additional details provided in the main chapter text.

4.1 β-SWAP Operator

Panel **(a)** of Figure 4.1 shows the Rabi-Chevron pattern for the $\hat{U}_\beta^{(1)}$ operator of the β-SWAP, realizing the $|g1\rangle \leftrightarrow |e0\rangle$ transition between the target qubit and coupler. Panel **(b)** displays the fitted Rabi frequency for each value of the modulation frequency $\omega_m^{(\beta_1)}$ in **(a)**. This takes the form of a quadratic function, with its minimum at the optimal frequency $\omega_{m,\star}^{(\beta_1)}$. Finally, panel **(c)** shows the cross section of the Rabi-oscillations for the optimal modulation frequency. The first extremum reveals a population transfer of 99.1 % for $|g1\rangle \to |e0\rangle$, after which the oscillations show a slightly decaying profile, corresponding to the $|e\rangle_q$ ($|1\rangle_c$) relaxation of the target (coupler). Thus, we choose the optimal pulse duration $\tau_{\beta,\star}^{(1)} = 66.0\,\text{ns}$, ultimately realizing $\hat{U}_\beta^{(1)}$. We also notice a minor fracture in the pattern for $\omega_m^{(\beta_1)} \approx 0.744\,\text{GHz}$, most likely suggesting a collision with another resonant mode around this frequency.

In analogue to Figure 4.1, panel **(a)** of Figure 4.2 shows the Rabi-Chevron pattern for $\hat{U}_\beta^{(2)}$, realizing the $|g2\rangle \leftrightarrow |e1\rangle$ transition between the target and coupler. Panel **(b)** again displays the fitted Rabi-oscillation frequency, from which we extract the optimal modulation frequency $\omega_{m,\star}^{(\beta_2)}$. The Rabi-oscillations for the optimal frequency in panel **(c)** reveals a population transfer of 99.9 % for $|g2\rangle \to |e1\rangle$. After this, the oscillations show a similar decaying profile, this time corresponding to the $|e\rangle_q$ ($|1\rangle_c$ and $|2\rangle_c$) relaxation of the target (coupler). To compensate for the different coupling rates, we divide the modulation amplitude of $\hat{U}_\beta^{(2)}$ by a factor $1.09\sqrt{2}$, agreeing well with the theoretical prediction of a $\sqrt{2}$ times faster $\hat{U}_\beta^{(2)}$ swap. This equalizes the effective rates of $\hat{U}_\beta^{(1)}$ and $\hat{U}_\beta^{(2)}$, resulting in $\tau_{\beta,\star}^{(2)} = 66.5\,\text{ns}$.

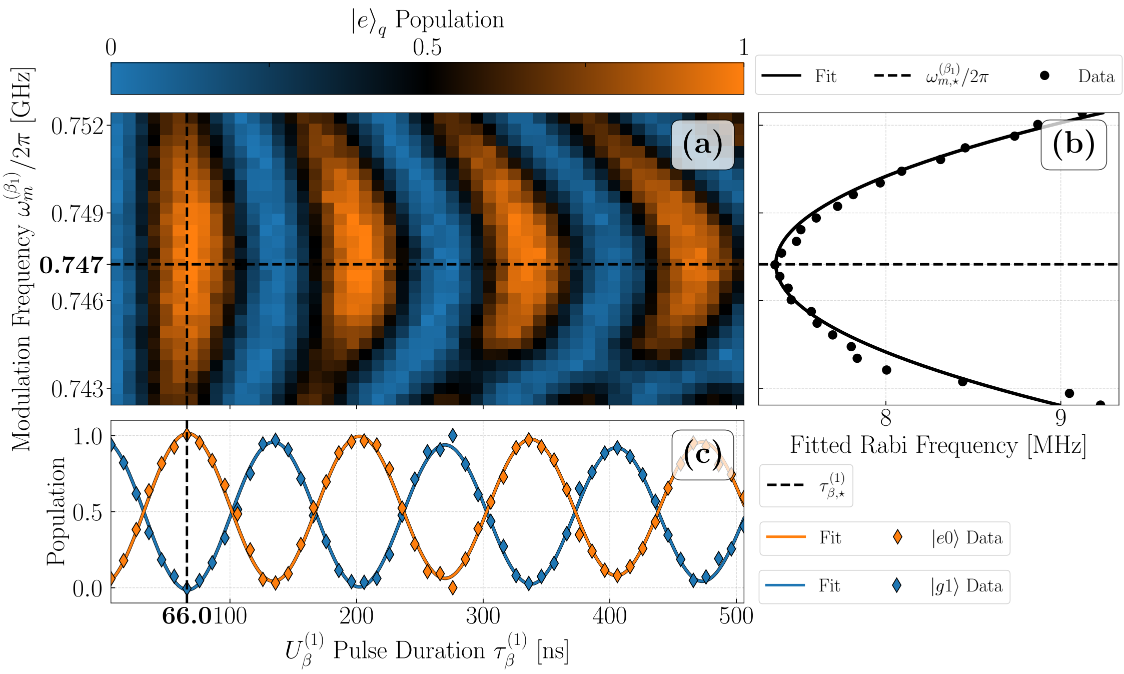

Figure 4.1: **(a)** Acquired Rabi-Chevron pattern for $\hat{U}_\beta^{(1)}$ when sweeping $\omega_m^{(\beta_1)}$ and $\tau_\beta^{(1)}$. **(b)** Fitted Rabi-oscillation frequencies for each $\omega_m^{(\beta_1)}$ in **(a)**. **(c)** State population as a function of $\tau_\beta^{(1)}$ for the optimal modulation frequency $\omega_{m,\star}^{(\beta_1)}$. The vertical line marks the shortest pulse length $\tau_{\beta,\star}^{(1)}$ that realizes the $\hat{U}_\beta^{(1)}$ term.

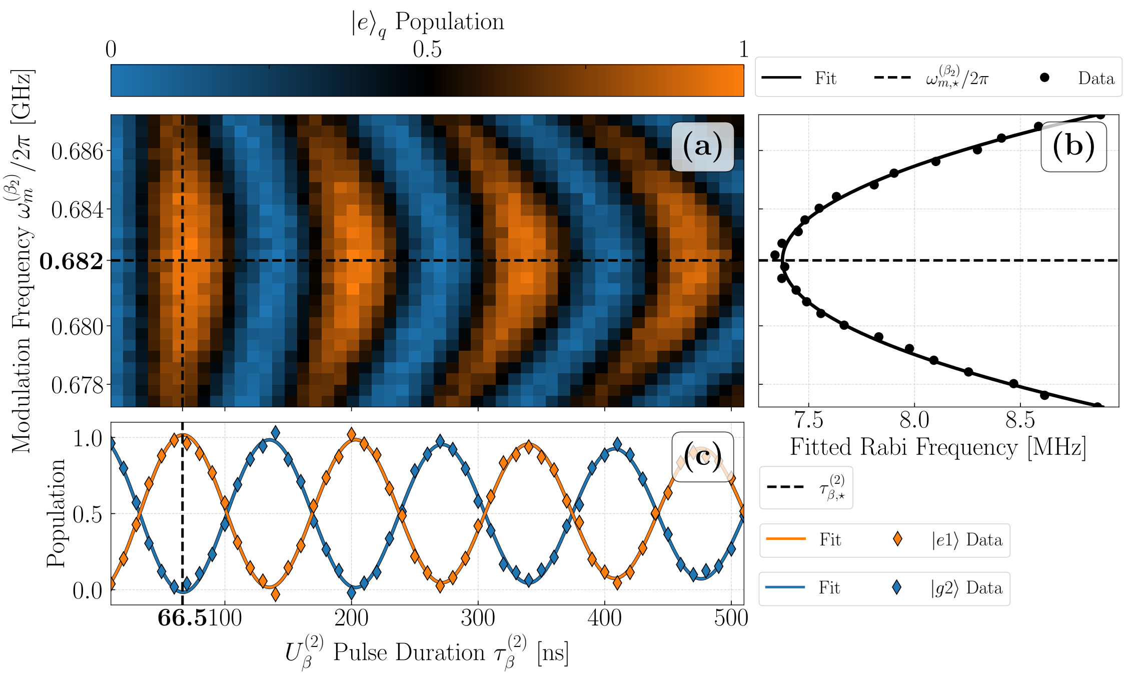

Figure 4.2: **(a)** Acquired Rabi-Chevron pattern for $\hat{U}_\beta^{(2)}$ when sweeping $\omega_m^{(\beta_2)}$ and $\tau_\beta^{(2)}$. **(b)** Fitted Rabi-oscillation frequencies for each $\omega_m^{(\beta_2)}$ in **(a)**. **(c)** State population as a function of $\tau_\beta^{(2)}$ for the optimal modulation frequency $\omega_{m,\star}^{(\beta_2)}$. The vertical line marks the shortest pulse length $\tau_{\beta,\star}^{(2)}$ that realizes the $\hat{U}_\beta^{(2)}$ term.

4.2 Re-thermalization of the Bosonic Mode

Figure 4.3 shows the results for resetting the coupler $|1\rangle_c$ state. The first three sidebands are visible, where the zoomed inset focuses on $n = 1$. Each point in the inset corresponds to the three possible decay regimes shown in the right panel. These are the **(b)** overdamped, **(c)** critically damped, and **(d)** underdamped regimes. The critically damped regime, which balanced decay is more predictable than that of the underdamped, shows a reset time of approximately 1 µs and a residual excited state population of around 1 %. This is a significant decay speedup compared to the regular $|1\rangle_c \to |0\rangle_c$ reset rate of $T_1^c \approx 15\,\mu s$.

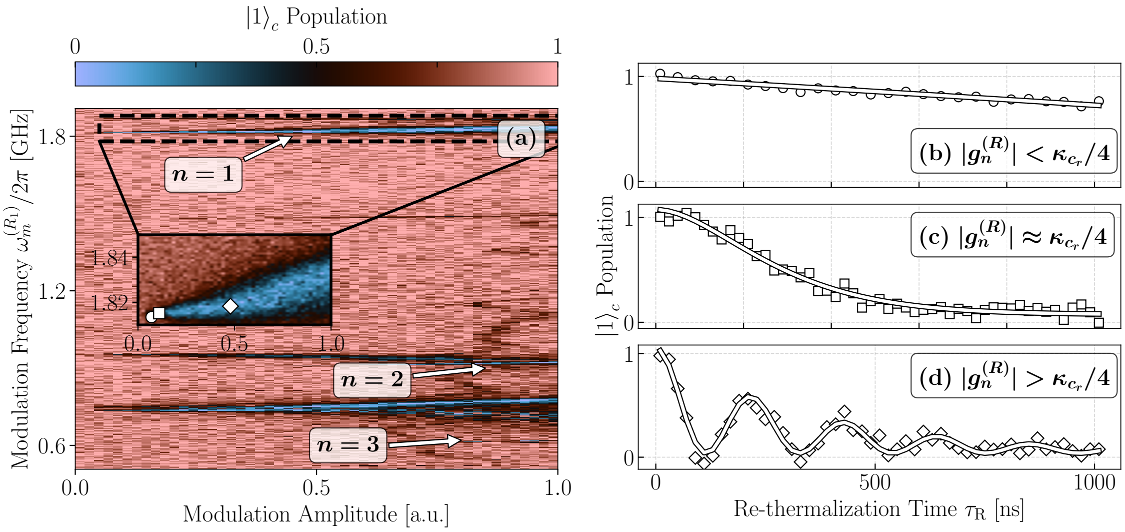

Figure 4.3: **(a)** Population of the coupler $|1\rangle_c$ state when sweeping the modulation amplitude and frequency $\omega_m^{(R_1)}$. The inset shows a zoomed view of the first sideband $n = 1$, with points corresponding to the three different decay regimes marked. The right panel displays the decay for each point on the inset in **(a)**, namely the **(b)** overdamped, **(c)** critically damped, and **(d)** underdamped regime.

Secondly, Figure 4.4 shows the result for resetting both $|1\rangle_c$ and $|2\rangle_c$ simultaneously. Panel **(a)** shows the raw readout response for sweeping the modulation frequencies $\omega_m^{(R_1)}$ and $\omega_m^{(R_2)}$ when starting in $|2\rangle_c$. Here, several of the resonance regions described in Section 3.3.2 are visible, where the zoomed inset shows the region where we find the optimal frequencies for realizing the reset. Panels **(b)** and **(c)** show the population of the $|0\rangle_c$ and $|2\rangle_c$ states, respectively, together with the same inset as in **(a)**. In this area, we indeed see a reduced $|2\rangle_c$ population, while the ground state population approaches 1. Figure 4.5 finally shows the excited state population (i.e., both $|1\rangle_c$ and $|2\rangle_c$) as a function of the reset pulse duration for the optimal modulation frequencies. We notice a total reset time of 3 µs and a residual excited state population of 4.1 %.

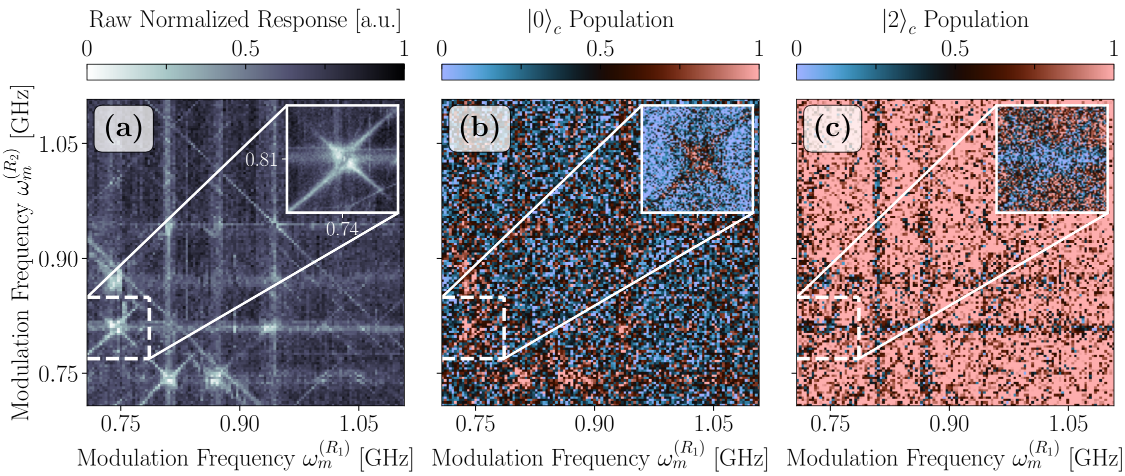

Figure 4.4: **(a)** Normalized response from sweeping the reset modulation frequencies $\omega_m^{(R_1)}$ and $\omega_m^{(R_2)}$ when starting in $|2\rangle_c$. **(b)** Population of the coupler $|0\rangle_c$ state. **(c)** Population of the coupler $|2\rangle_c$ state. The zoomed-in insets show the region where we find the optimal modulation frequencies for realizing the $|2\rangle_c \rightarrow |0\rangle_c$ reset.

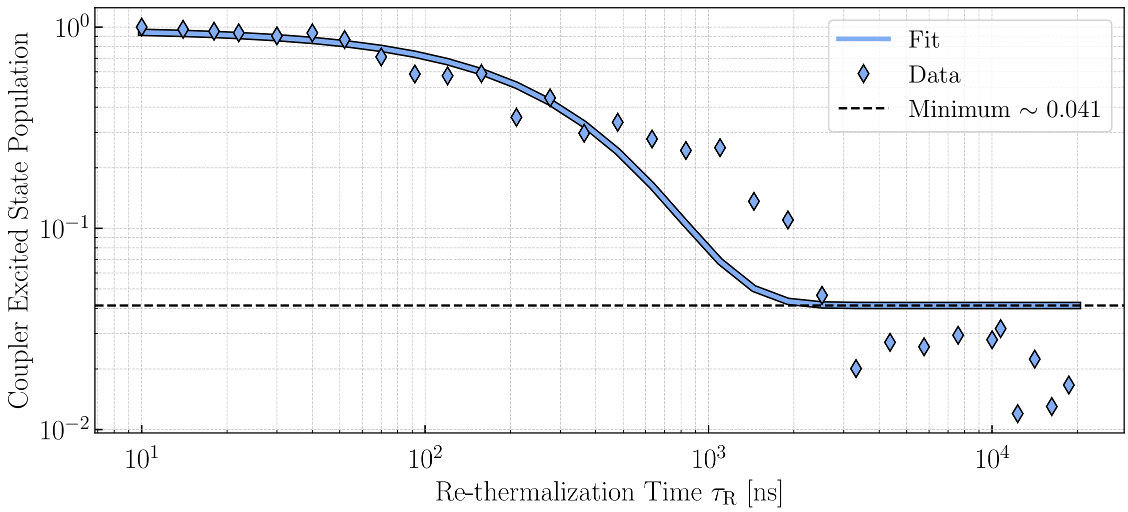

Figure 4.5: The coupler excited state population as a function of the reset time τ_R for the optimal modulation frequencies chosen from Figure 4.4.

4.3 Extended HBAC Implementation

Figure 4.6 shows the thermal population of the target qubit, P_{th}^q, as a function of the first five extended HBAC iterations when only employing the $\hat{U}_\beta^{(1)}$ term of the β-SWAP, compared to theoretical simulations. Panel **(a)** displays the result when the coupler $|1\rangle_c$ state was reset in between $\hat{U}_\beta^{(1)}$ operations, while panel **(b)** does not use reset. There is a clear mismatch between data and theory, and no cooling effect can generally be observed.

The result in panel **(a)** suggests that the reset works to some extent, as it prohibits the thermal population from reaching higher values. Specifically, we expect the thermal population to oscillate when not employing reset since this will result in a closed system, where the entropy (population) will circle around the system, as explained in Section 2.4.2.1. When including reset, the entropy is dissipated to the coupler resonator, instead allowing the thermal population to saturate, as seen in the figure below. On the other hand, the data in panel **(b)**, obtained without reset, seems closer to theory, suggesting that the reset protocol is not completely perfect.

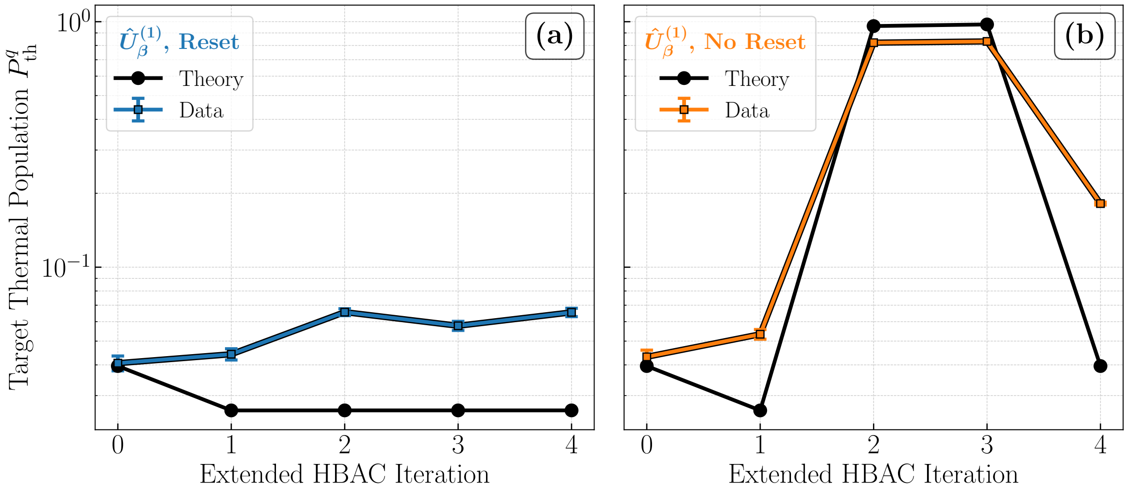

Figure 4.6: Thermal population of the target qubit as a function of the first five extended HBAC iterations, **(a)** with and **(b)** without reset of the coupler $|1\rangle_c$ state when employing the first β-SWAP term $\hat{U}^{(1)}_\beta$.

Similarly, Figure 4.7 shows P^q_{th} when employing both $\hat{U}^{(1)}_\beta$ and $\hat{U}^{(2)}_\beta$, with **(a)** and without **(b)** reset of the coupler $|1\rangle_c$ state. Again, the experimental data does not match the theoretical prediction and no cooling effect is observed. The reset also tends to work in this case, where the thermal population is confined to lower numbers compared to the non-reset case, as discussed earlier. However, the saturating thermal population is now higher than in the previous case, when only $\hat{U}^{(1)}_\beta$ was used. This observation again suggests that the reset protocol is not perfect, and most likely fails to reset both coupler states perfectly, leading to higher final thermal populations. Considering the 4.1 % residual thermal population in this case, compared to 1 % in the first case, this hypothesis becomes even more likely.

Finally, in both cases, we note that the initial P^q_{th} is consistent with the theoretical value at 70 mK, at which the experiments were performed. Furthermore, the almost negligible size of the error bars for all configurations suggests that the thermal population measurements are consistent across the different iterations. This indicates that the theory and experiment mismatch is not due to random fluctuations, but more likely a systematic issue in the implementation of the complete extended HBAC protocol. We hypothesise on what could be the cause for it in Chapter 5.

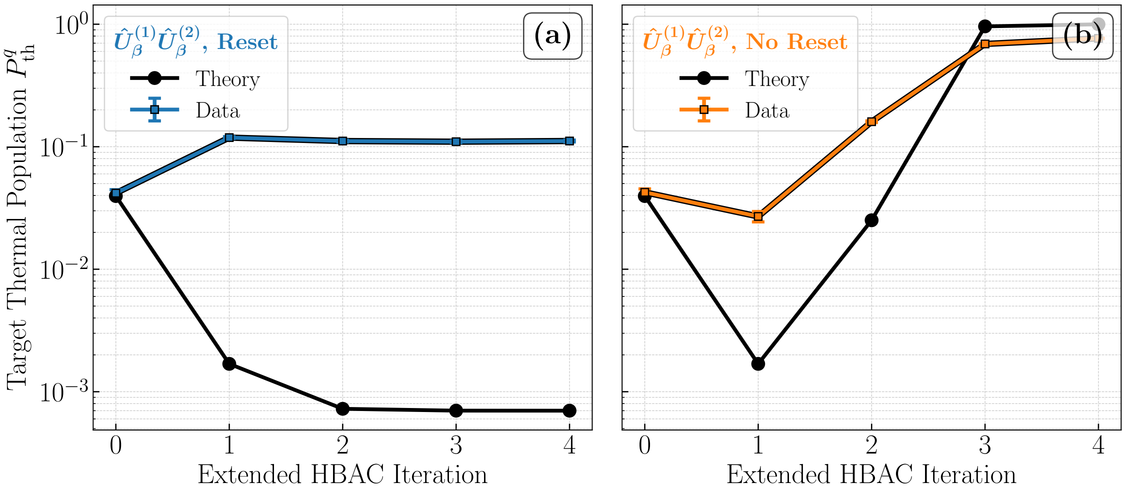

Figure 4.7: Thermal population of the target qubit as a function of the first five extended HBAC iterations, **(a)** with and **(b)** without reset of the coupler $|1\rangle_c$ and $|2\rangle_c$ states when employing the first two β-SWAP terms $\hat{U}_\beta^{(1)}$ and $\hat{U}_\beta^{(2)}$.

5

Discussion and Conclusion

This project has experimentally implemented the key building blocks of the extended HBAC protocol in a superconducting circuit and combined them into a first realization of the full experimental sequence. Using a rather generic device arrangement consisting of two qubits coupled through an intermediate coupler qubit, we show a truncated β-SWAP operator with at least 99 % population transfer between the target qubit and coupler. The optimal swap length of 66 ns is considerably smaller than the decay of the target qubit, which was a vital pre-requisite to achieve optimal cooling. Even though the demonstrated swap characteristics show promising dynamics for extended HBAC, there is potential for improvements in a future implementation. For instance, by operating at the coupler sweet spot, the effects of flux noise would be minimized, resulting in a more reliable β-SWAP through more stable modulation frequencies. Also, the coupler anharmonicity could be increased to allow more separation between $\hat{U}_\beta$ modulation frequencies, decreasing the risk of population leakage and thus resulting in a cleaner swap.

The resonator-assisted reset of the first excited state of the coupler, $|1\rangle_c$, exhibits a significant speedup compared to passive reset, decreasing from 15 µs to 1 µs, which is imperative for achieving optimal cooling. For the reset of both $|1\rangle_c$ and $|2\rangle_c$, we demonstrated a reset time of 3 µs. Considering the target qubit relaxation time $T_1^q = 37\,\mu\text{s}$, this should hold from a cooling perspective, even though it could be further decreased, as shown by Zhou et al. [36]. However, the minimum excited state population of 4 % is a more significant limitation, as this suggests that we do not completely reset the coupler in this case.

With this in mind, there are several aspects of the reset that could be improved. Firstly, the coupler readout was extremely noisy. In particular, the coupler χ was on the order of tens of kHz, which made it difficult to distinguish the different coupler states and accurately measure the reset performance. By increasing this value, the SNR could be improved significantly, allowing for a more reliable analysis of the reset procedure. Secondly, by increasing the decay rate of the coupler, the reset times could be further decreased, which would be beneficial for the cooling effect. This could for instance be achieved by using a different device design with a more lossy coupler. Lastly, no attempt of optimizing the modulation amplitude for the higher order reset was made. This could be tackled using some optimization algorithm, optimizing over the excited states population as cost function.

By ultimately combining the β-SWAP and re-thermalization, we realize the complete extended HBAC protocol. The results shows a clear mismatch between the experimental data and theoretical predictions, and no cooling effect is observed. However, the reset works to some extent, prohibiting the thermal population from reaching higher numbers. This suggests that the reset is not perfect, but still has a positive effect on the cooling performance. When it comes to possible error sources, the negligible error bars of the thermal population indicate that the lacking cooling performance is likely not due to random fluctuations, but rather systematic issues in the implementation of the complete protocol.

The main source of error for the complete implementation is the crosstalk between the target qubit and coupler. Since the protocol functions in the combined target-coupler subspace, state-dependent frequency shifts for the different qubits must be taken into account when calibrating pulses and performing readout. Using both $\hat{U}_\beta^{(1)}$ and $\hat{U}_\beta^{(2)}$, the protocol involves up to six different combined-systems states, each affecting the dynamics of the qubits differently. As an example, this especially affects the thermal population measurement, which includes several pulses that will be prone to the crosstalk. To handle this, the most straightforward solution would be to design a device where the CZ interaction between the target and coupler is minimized. Moreover, in the case of a better coupler readout, joint readout could be employed to analyze the performance of the β-SWAP more reliably.

Furthermore, even though the individual β-SWAP shows a solid population transfer, the discrepancy between theory and experiment, particularly in the case without reset, suggests that the swap is not perfect in the complete implementation. The most likely reason for this is the population leakage to higher levels of the qubits, specifically involving excited states of the target, which would decrease the cooling effect. To handle this, the swap pulse could be optimized to minimize the population of higher levels, for instance by using DRAG pulses or optimal control methods. Additionally, the device design could be modified to increase the anharmonicity of the coupler, which would increase the separation between the different $\hat{U}_\beta$ modulation frequencies and make it less likely for higher levels to be populated.

In conclusion, this thesis provides a proof-of concept of the extended HBAC implementation in a superconducting circuit by experimentally demonstrating and merging the key components. By optimizing the device characteristics and employing more sophisticated calibration techniques to handle protocol-specific error sources, the cooling effect could be enhanced and more accurately demonstrated. This would be an important step towards optimal qubit initialization of quantum systems, paving the way for the future of superconducting quantum technology.

Bibliography

[1] D. P. DiVincenzo, "The physical implementation of quantum computation," *Fortschritte der Physik*, vol. 48, no. 9–11, pp. 771–783, 2000. DOI: 10.1002/1521-3978(200009)48:9/11<771::AID-PROP771>3.0.CO;2-E

[2] P. O. Boykin, T. Mor, V. Roychowdhury, F. Vatan, and R. Vrijen, "Algorithmic cooling and scalable NMR quantum computers," *Proceedings of the National Academy of Sciences*, vol. 99, no. 6, pp. 3388–3393, 2002. DOI: 10.1073/pnas.241641898

[3] Á. M. Alhambra, M. Lostaglio, and C. Perry, "Heat-bath algorithmic cooling with optimal thermalization strategies," *Quantum*, vol. 3, p. 188, Sep. 2019, ISSN: 2521-327X. DOI: 10.22331/q-2019-09-23-188 [Online]. Available: http://dx.doi.org/10.22331/q-2019-09-23-188

[4] National Quantum Office (Singapore). "National quantum strategy (nqs)." Accessed: 2026-03-17. [Online]. Available: https://nqo.sg/nqs/

[5] Chalmers University of Technology. "Wallenberg centre for quantum technology (wacqt)." Accessed: 2026-03-17. [Online]. Available: https://www.chalmers.se/en/centres/wacqt/

[6] Google Quantum AI. "Quantum computing roadmap." Accessed: 2026-03-17. [Online]. Available: https://quantumai.google/roadmap

[7] Microsoft. "Microsoft quantum roadmap: Vision for scalable quantum computing." Accessed: 2026-03-17. [Online]. Available: https://quantum.microsoft.com/en-us/vision/quantum-roadmap

[8] IBM. "Ibm quantum roadmap to 2030 and beyond." Accessed: 2026-03-17. [Online]. Available: https://www.ibm.com/roadmaps/quantum/2030/

[9] J. Whalen, "Amazon joins race for quantum computer with new caltech center," *The Washington Post*, Oct. 2021, Accessed: 2026-03-17. [Online]. Available: https://www.washingtonpost.com/technology/2021/10/26/amazon-quantum-computer-caltech/

[10] M. Born and P. Jordan, "Zur quantenmechanik," *Zeitschrift für Physik*, vol. 34, pp. 858–888, 1925. DOI: 10.1007/BF01328531

[11] R. P. Feynman, "Simulating physics with computers," *International Journal of Theoretical Physics*, vol. 21, no. 6–7, pp. 467–488, 1982.

[12] P. W. Shor, "Polynomial-time algorithms for prime factorization and discrete logarithms on a quantum computer," *SIAM Journal on Computing*, vol. 26, pp. 1484–1509, Oct. 1997, ISSN: 1095-7111. DOI: `10.1137/s0097539795293172` [Online]. Available: `http://dx.doi.org/10.1137/S0097539795293172`

[13] L. K. Grover, *A fast quantum mechanical algorithm for database search*, 1996. arXiv: `quant-ph/9605043 [quant-ph]`. [Online]. Available: `https://arxiv.org/abs/quant-ph/9605043`

[14] F. Arute et al., "Quantum supremacy using a programmable superconducting processor," *Nature*, vol. 574, pp. 505–510, 2019. DOI: `10.1038/s41586-019-1666-5`

[15] H. Soller, M. Gschwendtner, S. Shabani, and W. Svejstrup, "The year of quantum: From concept to reality in 2025," McKinsey & Company, Jun. 2025, Fourth annual Quantum Technology Monitor report estimating the future size of the quantum technology market worldwide. [Online]. Available: `https://www.mckinsey.com/capabilities/tech-and-ai/our-insights/the-year-of-quantum-from-concept-to-reality-in-2025`

[16] K. Geerlings et al., "Demonstrating a driven reset protocol for a superconducting qubit," *Physical Review Letters*, vol. 110, no. 12, p. 120 501, Mar. 2013. DOI: `10.1103/PhysRevLett.110.120501` [Online]. Available: `https://doi.org/10.1103/PhysRevLett.110.120501`

[17] P. Magnard et al., "Fast and unconditional all-microwave reset of a superconducting qubit," *Physical Review Letters*, vol. 121, no. 6, p. 060 502, Aug. 2018. DOI: `10.1103/PhysRevLett.121.060502` [Online]. Available: `https://doi.org/10.1103/PhysRevLett.121.060502`

[18] D. Ristè, C. C. Bultink, K. W. Lehnert, and L. DiCarlo, "Feedback control of a solid-state qubit using high-fidelity projective measurement," *Physical Review Letters*, vol. 109, no. 24, p. 240 502, Dec. 2012. DOI: `10.1103/PhysRevLett.109.240502` [Online]. Available: `https://doi.org/10.1103/PhysRevLett.109.240502`

[19] Y. Salathé et al., "Low-latency digital signal processing for feedback and feedforward in quantum computing and communication," *Physical Review Applied*, vol. 9, no. 3, p. 034 011, Mar. 2018. DOI: `10.1103/PhysRevApplied.9.034011` [Online]. Available: `https://doi.org/10.1103/PhysRevApplied.9.034011`

[20] M. A. Aamir, P. Jamet Suria, J. A. Marín Guzmán, et al., "Thermally driven quantum refrigerator autonomously resets a superconducting qubit," *Nature Physics*, vol. 21, pp. 318–323, 2025. DOI: `10.1038/s41567-024-02708-5`

[21] L. J. Schulman and U. V. Vazirani, "Molecular scale heat engines and scalable quantum computation," in *Proceedings of the Thirty-First Annual ACM*

Symposium on Theory of Computing, ACM, 1999, pp. 322–329. DOI: `10.1145/301250.301332`

[22] H. K. Onnes, "The superconductivity of mercury," *Communications from the Physical Laboratory of the University of Leiden*, vol. 122, pp. 1–4, 1911.

[23] R. P. Feynman, R. B. Leighton, and M. Sands, *The Feynman Lectures on Physics, Vol. III: Quantum Mechanics*. San Francisco: Pearson Addison-Wesley, 2006.

[24] J. Bardeen, L. N. Cooper, and J. R. Schrieffer, "Theory of superconductivity," *Physical Review*, vol. 108, no. 5, pp. 1175–1204, 1957. DOI: `10.1103/PhysRev.108.1175`

[25] A. Bergen et al., "Design and in-field testing of the world's first rebco rotor for a 3.6 mw wind generator," *Superconductor Science and Technology*, vol. 32, no. 12, p. 125 006, 2019. DOI: `10.1088/1361-6668/ab48d6`

[26] Nobel Prize Outreach. "The nobel prize in physics 1973." Accessed: 2026-03-17. [Online]. Available: `https://www.nobelprize.org/prizes/physics/1973/summary/`

[27] B. D. Josephson, "Possible new effects in superconductive tunnelling," *Physics Letters*, vol. 1, no. 7, pp. 251–253, Jul. 1962. DOI: `10.1016/0031-9163(62)91369-0`

[28] H.-P. Breuer and F. Petruccione, *The Theory of Open Quantum Systems*. Oxford: Oxford University Press, 2007, ISBN: 9780199213900. DOI: `10.1093/acprof:oso/9780199213900.001.0001`

[29] A. Blais, R.-S. Huang, A. Wallraff, S. M. Girvin, and R. J. Schoelkopf, "Cavity quantum electrodynamics for superconducting electrical circuits: An architecture for quantum computation," *Physical Review A*, vol. 69, no. 6, Jun. 2004, ISSN: 1094-1622. DOI: `10.1103/physreva.69.062320` [Online]. Available: `http://dx.doi.org/10.1103/PhysRevA.69.062320`

[30] P. Krantz, M. Kjaergaard, F. Yan, T. P. Orlando, S. Gustavsson, and W. D. Oliver, "A quantum engineer's guide to superconducting qubits," *Applied Physics Reviews*, vol. 6, no. 2, Jun. 2019, ISSN: 1931-9401. DOI: `10.1063/1.5089550` [Online]. Available: `http://dx.doi.org/10.1063/1.5089550`

[31] Y. Nakamura, Y. A. Pashkin, and J. S. Tsai, "Coherent control of macroscopic quantum states in a single-cooper-pair box," *Nature*, vol. 398, pp. 786–788, 1999. DOI: `10.1038/19718`

[32] J. Koch et al., "Charge-insensitive qubit design derived from the cooper pair box," *Physical Review A*, vol. 76, p. 042 319, 2007. DOI: `10.1103/PhysRevA.76.042319`

[33] M. Kjaergaard et al., "Superconducting qubits: Current state of play," *Annual Review of Condensed Matter Physics*, vol. 11, no. 1, pp. 369–395, Mar. 2020, ISSN: 1947-5462. DOI: `10.1146/annurev-conmatphys-031119-050605` [On-

line]. Available: http://dx.doi.org/10.1146/annurev-conmatphys-031119-050605

[34] N. Didier, E. A. Sete, M. P. da Silva, and C. Rigetti, "Analytical modeling of parametrically modulated transmon qubits," *Physical Review A*, vol. 97, no. 2, Feb. 2018, ISSN: 2469-9934. DOI: 10.1103/physreva.97.022330 [Online]. Available: http://dx.doi.org/10.1103/PhysRevA.97.022330

[35] M. Reagor et al., "Demonstration of universal parametric entangling gates on a multi-qubit lattice," *Science Advances*, vol. 4, no. 2, aao3603, Feb. 2018. DOI: 10.1126/sciadv.aao3603

[36] Y. Zhou et al., "Rapid and unconditional parametric reset protocol for tunable superconducting qubits," *Nature Communications*, vol. 12, no. 1, Oct. 2021, ISSN: 2041-1723. DOI: 10.1038/s41467-021-26205-y [Online]. Available: http://dx.doi.org/10.1038/s41467-021-26205-y

[37] Bluefors, *LD System: Dilution Refrigerator Measurement System*, https://bluefors.com/products/dilution-refrigerator-measurement-systems/ld-dilution-refrigerator-measurement-system/, Accessed: 2026-05-14.

[38] Intermodulation Products AB, *Presto: Microwave arbitrary waveform generator and analyser*, Accessed: 2026-05-14, Intermodulation Products AB, 2026. [Online]. Available: https://www.intermod.pro/products/microwave-platforms

[39] Intermodulation Products AB, *Presto 2.17.0 documentation*, Accessed: 2026-05-14, Intermodulation Products AB, 2026. [Online]. Available: https://intermod.pro/manuals/presto/

[40] S. Probst, F. B. Song, P. A. Bushev, A. V. Ustinov, and M. Weides, "Efficient and robust analysis of complex scattering data under noise in microwave resonators," *Review of Scientific Instruments*, vol. 86, no. 2, Feb. 2015, ISSN: 1089-7623. DOI: 10.1063/1.4907935 [Online]. Available: http://dx.doi.org/10.1063/1.4907935

DEPARTMENT OF MICROTECHNOLOGY AND NANOSCIENCE
CHALMERS UNIVERSITY OF TECHNOLOGY
Gothenburg, Sweden
www.chalmers.se

AVANCEZ
1829
CHALMERS
UNIVERSITY OF TECHNOLOGY